IEEE Access
Multidisciplinary | Rapid Review | Open Access Journal

Received July 12, 2019, accepted August 4, 2019, date of publication August 14, 2019, date of current version September 11, 2019.

Digital Object Identifier 10.1109/ACCESS.2019.2934859

Numerical Study on the Hydrodynamic Characteristics and Responses of Moored Floating Marine Cylinders Under Real-World Tsunami-Like Waves

ENJIN ZHAO[1,2,3], JUNKAI SUN[1], HAOYU JIANG[1,2,3], AND LIN MU[1,3]

[1]College of Marine Science and Technology, China University of Geosciences, Wuhan 430074, China
[2]Laboratory for Regional Oceanography and Numerical Modeling, Qingdao National Laboratory for Marine Science and Technology, Qingdao 266237, China
[3]Shenzhen Research Institute, China University of Geosciences, Shenzhen 518057, China

Corresponding author: Lin Mu (moulin1977@hotmail.com)

This work was supported in part by the National Key Research and Development Program of China under Grant 2017YFC1404700, in part by the National Natural Science Foundation of China under Grant 41806010, in part by the Laboratory for Regional Oceanography and Numerical Modeling, Qingdao National Laboratory for Marine Science and Technology, under Grant 2019A03, in part by the Discipline Layout Project for the Basic Research of Shenzhen Science and Technology Innovation Committee under Grant 20170418, and in part by the Guangdong Special Fund Program for Marine Economy Development under Grant GDME-2018E001.

ABSTRACT In recent tsunami events like those happened in the Indian Ocean in 2004 and 2018 and in Japan in 2011, many ocean and coastal infrastructures have been damaged tremendously, revealing the need of the work to study the hydrodynamic interaction between real-world tsunami waves and offshore structures. Besides, the destructive energy of tsunami wave on the offshore structures should also be assessed. However, to study the impact of tsunami waves on offshore structures, solitary waves are used generally instead of real-world tsunami waves despite the vast differences in hydrodynamic characteristics. Using Computational Fluid Dynamics (CFD) approach, this paper investigates the hydrodynamic characteristics of the floating cylinders moored by chains, under the real-world tsunami-like waves (2011 Japan Tohoku tsunami). Comparisons of hydrodynamic characteristics between real-world tsunami-like wave and solitary wave propagating over the moored cylinders are analyzed and discussed, indicating that the flow fields, the tension forces of mooring chains, the impinging forces and the movement trajectories of the cylinder caused by the two types of waves are greatly different from each other. Moreover, the influences of single cylinder diameter and tandem cylinder spacing on the interaction between real-world tsunami-like waves and cylinders are considered through a series of simulation tests, while meaningful conclusions are drawn.

INDEX TERMS Hydrodynamic characteristics, moored cylinder, real-world tsunami-like wave, solitary wave, hydrodynamic forces.

I. INTRODUCTION

Due to submarine earthquakes, landslides, volcanic and other disturbances above or below the sea water, a substantial volume of water might fluctuate severely which would induce a series of water waves. The wave height increases while the wave length and speed decrease when the water wave spreads to coastal area, resulting in the phenomenon of tsunami. Tsunami can cause severe damages to industrial equipment, buildings and offshore structures, leading to serious world safety threats and huge economic losses [1]–[3]. The tsunami events happened in Japan in 2011 brought about destructions of 30% of the responding industrial facilities. Therefore, it is urgent to understand the fundamental damaging mechanisms to increase the resilience of the infrastructures during tsunami events.

Concerning the impact of tsunami waves, many researches have been carried out from various perspectives. In some researches [4]–[8], the physical modelling of tsunami wave and the application of the tsunami wave have been developed and carried out, which reveals some significant mechanism about tsunami. Solitary wave is generally employed as the tsunami wave [9]–[11]. Aniel-Quiroga *et al.* (2018) conducted a series of laboratory experiments on scaled models of

The associate editor coordinating the review of this article and approving it for publication was Giovanni Angiulli.

two typical Mediterranean rubble-mound breakwater typologies under tsunami waves. In this research, the action of tsunami wave was split into two parts: (1) the first impact of tsunami wave was caused by means of the large solitary wave; (2) the subsequent overflow was approached by applying a pump-driven wave maker [12]. Ha *et al.* (2014) studied three-dimensional numerical simulation of solitary wave using the immersed boundary (IB) method [13]. However, due to the survey of the real-world tsunami wave, solitary waves rarely happen in the tsunami events [14]. According to the record of the Iwate South station from the 2011 Tohoku Japan tsunami, this tsunami wave is observed as a leading-depression wave firstly, which induces the decrease of sea level. Then, with the propagation of the tsunami wave, the elevation of the wave surface increases depending on the profile of the tsunami wave. The evolution of the tsunami wave is completely different with solitary wave at the temporal and spatial scales [15], [16]. Chan and Liu (2012) suggested that a reasonable estimation of the water run up under tsunami wave should depend on a reliable characterization of the tsunami wave. The solitary wave is more distinct from the real-world tsunami wave in the period and shape. So, some researchers implied that the study of the interaction between the structure and tsunami wave should use the observed tsunami wave profile rather than the solitary wave. In order to describe the tsunami wave reasonably, N-wave is introduced which consists of a superposition of the negative and positive single wave. According to the concept of N-wave, the tsunami wave recorded at Iwate South station during the 2011 Japan Tohoku tsunami is calculated and replicated using a combination of three $\mathrm{sech}^2(*)$ profiles [17]. The proposed real-world tsunami-like wave has been employed to investigate the tsunami-scale wave boundary layer and the water run-up in the coast [18].

When the tsunami waves impact on offshore structures, the hydrodynamic loads might exceed the design limit instantaneously, leading to irreversible strength damage or loss of overall balance of structures. Also, propagation of the wave might cause a large displacement of the structure and the severe heave motion of floating offshore platforms. It is noticed that many basic components of offshore structures are shaped as circular cylinders, such as marine pipeline, platform buoy and wave buoy. Therefore, studying on hydrodynamic characteristics of cylinders under tsunami waves is gradually attracted by researchers. Qu *et al.* (2017) numerically studied the impact of tsunami wave at submerged horizontal cylinders. It is estimated that the tsunami wave loads increase monotonously with wave height. The tsunami wave can cause about 10% and 16% higher than solitary wave for horizontal and vertical loads, respectively. However, in the research, the cylinders are fixed in the water. The motion characteristics of the cylinders in tsunami wave cannot be estimated. Understanding of the object drift behavior is very important for engineering purposes [19]. Wadhams (1983) pointed out that the wave-induced drift can be a dominating factor in the movement of the marine structures, even under strong wind. Besides, in order to limit the large movement of various floating objects, the objects are restricted by the mooring system using the chain which is the other essential portion of the marine structure. In the extreme environmental conditions, the mooring chains can stabilize the strenuous movement of the floating objects. Thus, the research on the tension force of the mooring chain under tsunami wave is also important [20].

Since the hydrodynamic characteristics of tsunami wave and solitary wave are quite unlike, the effect of real-world tsunami wave on the offshore structures also differs from that of solitary wave. However, existing research seldom considers the real-world tsunami waves. This paper analyzes and discusses the effects of the real-world tsunami-like wave acting on moored cylinders in detail using CFD simulation method. The numerical solver in this paper solves the incompressible Navier-Stokes equations discretized with Finite Volume Method (FVM) [21], [22], and captures the free surface using the Volume of Fluid (VOF) method. The numerical model is verified by two experimental cases from aspects of the drifting trajectory and the hydrodynamic loads respectively. Systematic study of the real-world tsunami-like wave acting on moored cylinders is conducted after the validation. The comparison of the hydrodynamic characteristics between cylinders under the tsunami-like wave and a solitary wave with same wave height is given, demonstrating remarkable differences on the movement trajectory of the cylinder and the wave impinging forces. Furthermore, the effects of single cylinder diameter and tandem cylinder spacing are also investigated, from which meaningful conclusions are summed up.

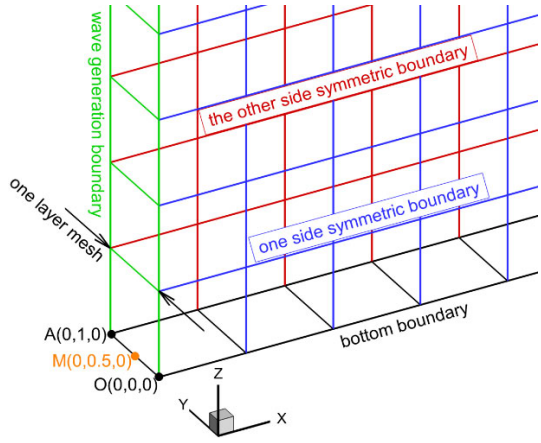

FIGURE 1. The sketch of simulation mesh.

II. NUMERICAL METHODOLOGY

A. NUMERICAL SOLVER OF THE FLUID DOMAIN

In the numerical model, the flow region is subdivided into a mesh of fixed rectangular cells. As shown in Fig. 1, the simulation is 2D in x- and z-directions. In y-direction, one mesh layer should be given and there still is a distance between two symmetric boundaries in this one-layer mesh which has

coordinate values in space. The obstacles are embedded in the mesh by defining the fractional volumes of the cells that are open to flow.

The RANS equations (Reynolds-averaged Navier–Stokes equations) are used in the simulation, including the continuity and momentum equations for the fluid flow.

$$\nabla \cdot (A\mathbf{u}) = 0 \tag{1}$$

$$\frac{\partial \mathbf{u}}{\partial t} + \frac{1}{V_f}\nabla \cdot (A\mathbf{u}\mathbf{u}) = -\frac{1}{\rho}\nabla \cdot p + \mathbf{G} + \mathbf{F} \tag{2}$$

where $\mathbf{u}$ is the velocity vector, A is fractional area for flow in x-, y- or z-direction, t is the time, V_f is the fractional volume for flow, ρ is the water density, p is the pressure, $\mathbf{G}$ is the body acceleration vector, $\mathbf{F}$ is the viscous acceleration vector.

The interface between water and air is defined in terms of a volume of fluid (VOF) function, and the transport equation of volume of fluid can be written as:

$$\frac{\partial \gamma}{\partial t} + \frac{1}{V_f}\nabla \cdot (\gamma A\mathbf{u}) = 0 \tag{3}$$

where γ is the volume fraction of water in a cell, defined by the control volume filled by water or air. The control equations are expressed as:

$$\gamma = \begin{cases} \gamma = 0, & air \\ 0 < \gamma < 1, & interface \\ \gamma = 1, & water \end{cases} \tag{4}$$

In the model, the conversation equations are closed by κ-ω turbulence model. The collocated finite volume method is applied to discretize the continuity and momentum equations, and the deferred correction is employed to discretize the convective terms by combining the first-order upwind scheme and the second-order Gamma scheme. The diffusion and pressure terms are approximated as the central difference. In order to couple the continuity and momentum equations, the momentum interpolation method is adopted to interpolate the velocities of the control cell centers to the control cell faces [23], while the velocities and pressures are decoupled by the Pressure Implicit Split Operator (PISO) method [24]. The sharpness of the free surface between the water and air is controlled by the high-resolution VOF method named Switching Technique for Advection and Capturing of Surfaces (STACS) [25].

B. GENERATION OF REAL-WORLD TSUNAMI-LIKE WAVES

In the simulation, the wave prototype is recorded at Iwate South station during the 2011 Tohoku tsunami in Japan. The real-world tsunami wave is replicated depending on the N-wave theory. In the rest of the paper, the replicated real-world tsunami wave is abbreviated as tsunami-like wave.

In the simulation domain, the wave is generated at the wave generation boundary where the control conditions are defined with the free surface elevation and the wave velocity in Cartesian coordinate system. The wave propagates in the normal direction. Based on the boundary wave generation method, both the solitary wave and tsunami-like waves are numerically generated.

The wave elevation η of solitary wave on still water depth h can be expressed as

$$\eta(x, t) = H_o \mathrm{sech}^2[k_o(x - x_o - C_o t)] \tag{5}$$

where H_o is the wave height, $k_o = (3H_o/4h^3)^{1/2}$ is the effective wave number, x_o is the location of the wave crest at $t = 0$, $C_o = [g(H_o + h)]^{1/2}$ denotes the wave speed.

To produce the real-world tsunami wave, a combination of three $\mathrm{sech}^2(*)$ wave profiles is adopted to model the tsunami wave based on the concept of N-wave. The combination of three $\mathrm{sech}^2(*)$ wave could be written as:

$$\eta(x_i, t) = \sum_{i=1}^{3} H_i \mathrm{sech}^2[\omega_i(t - (t_o + t_i))] \tag{6}$$

where ω_i is the wave frequency of every $\mathrm{sech}^2(*)$ wave.

The parameters of the tsunami-like wave presented in previous researches of [16], [18] have been non-dimensionalized as follows:

$$\begin{aligned} (\frac{H_1}{H_o} \quad \frac{\omega_1}{\omega_o} \quad \frac{t_1}{T_o}) &= (-0.119 \quad 0.0856 \quad 6.556) \\ (\frac{H_2}{H_o} \quad \frac{\omega_2}{\omega_o} \quad \frac{t_2}{T_o}) &= (0.328 \quad 0.0947 \quad 8.776) \\ (\frac{H_3}{H_o} \quad \frac{\omega_3}{\omega_o} \quad \frac{t_3}{T_o}) &= (0.873 \quad 0.31244 \quad 10.54) \end{aligned} \tag{7}$$

where ω_o is the wave frequency of a solitary wave with the same wave height as tsunami-like wave. It is noted that in formula 7, the non-dimensional items consist of the wave height, wave frequency and the wave duration, which involves not only the scaling of spatial scale, but also the scaling of the temporal scale. So, in the generation of the tsunami-like wave, both the spatial scale and temporal scale have been related.

In the inlet boundary, the velocity of the wave is given by:

$$\boldsymbol{u}_i = \boldsymbol{C}_i \eta_i / (h + \eta_i) \tag{8}$$

$$\boldsymbol{u} = \sum_{i=1}^{3} \boldsymbol{u}_i \tag{9}$$

where $\boldsymbol{u}_i$ is the velocity vector of every $\mathrm{sech}^2(*)$ wave and $\boldsymbol{u}$ is the combination velocity vector in the inlet boundary. In Fig. 2, the wave profile comparison among observed tsunami-wave, tsunami-like wave and solitary wave is displayed. The observed tsunami wave presented by small black circles is recorded at Iwate station in 2011 Japan Tohoku tsunami event. The tsunami-like wave presented by red solid line is generated using a combination of three sech2(*) wave profiles depending on the N-shaped wave theory. And a general solitary wave presented by blue dash line is described with the same height as the peak of tsunami-like wave [26]. The parameters of three sech2(*) wave profiles are $H_i = [-0.8, 2.2, 5.85]$ m, $\omega_i = [0.179, 0.198, 0.653]$ min^{-1} and $t_i = [9.67, 16.33, 21.63]$ min, respectively. Through the comparison between the tsunami-like wave and observed tsunami

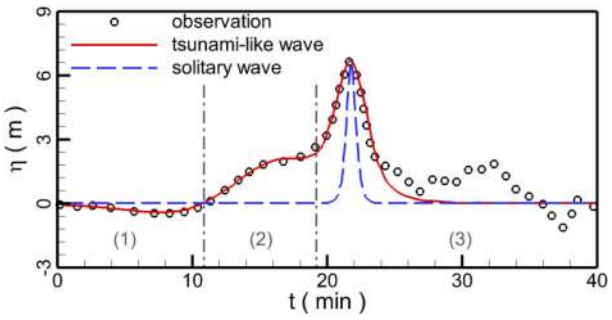

FIGURE 2. Wave profile comparison among observed tsunami wave, tsunami-like wave and solitary wave.

wave in Fig. 2, it is observed that the observed tsunami wave profile is accurately represented by tsunami-like wave which can capture (1) the leading-depression, (2) the preceding elevated and (3) the secondary elevated wave portions very well. Also, the solitary wave profile differs drastically from the tsunami wave. Apparently, the period and length of the tsunami-like wave are much longer than that of the solitary wave. A solitary wave is not the proper wave model for the tsunami wave study if results corresponding to actual tsunami waves are desired. In order to investigate the effects of real-world tsunami wave on the marine structures, a tsunami-like wave is used as the generation of tsunami wave instead of solitary wave to impinge the moored floating marine cylinders.

C. CYLINDER MOTION AND WAVE

Based on the location of the object, the volume fraction of the structured mesh is recalculated at each time step. Source terms of the cylinder motion are added in the continuity equation and the VOF transport equation. The hydraulic forces including hydrostatic pressure, hydrodynamic pressure and shear stress on the moving object are calculated. For convenience of computation, a body system (x′, y′, z′) is set up for moving object with its coordinate axes parallel to those of the space system (x, y, z) at time $t = 0$. The origin of the body system is set at the object mass center G. The body system is fixed on the moving object and experiences the same translation and rotation as the moving object. Coordinate transformation between the space system (x, y, z) and the body system (x′, y′, z′) is

$$\mathbf{X}_s = [R] \cdot \mathbf{X}_b + \mathbf{X}_G \tag{10}$$

where $\mathbf{X}_s$ and $\mathbf{X}_b$ are position vectors of a point in space and body systems, respectively. $\mathbf{X}_G$ is position vector of mass center in space system, and $[R]$ is an orthogonal coordinate transformation tensor

$$[R] = \begin{bmatrix} R_{11} & R_{12} & R_{13} \\ R_{21} & R_{22} & R_{23} \\ R_{31} & R_{32} & R_{33} \end{bmatrix} \tag{11}$$

where $R_{ij}R_{jk} = \delta_{ik}$ is the Kronecker δ symbol.

It is noted that the motion of the object is related to the object velocity, the velocity of any point on a rigid body is equal to the velocity of the object mass center G plus velocity due to rotation about the mass center with six-DOF motion. Denoting P as any point on the object, its velocity is related to the mass center velocity $\mathbf{V}_G$ and angular velocity ω of the rigid body by

$$\mathbf{V}_s = \mathbf{V}_G + \omega \times \mathbf{r}_{P/G} \tag{12}$$

where $\mathbf{r}_{P/G}$ is the distance vector from point G to point P.

When the object moves in the water, the object motion equations are separated two parts:

$$\mathbf{F} = m\frac{d\mathbf{V}_G}{dt} \tag{13}$$

$$\mathbf{T}_G = [J] \cdot \frac{d\omega}{dt} + \omega \times ([J] \cdot \omega) \tag{14}$$

where $\mathbf{F}$ is the total force, m is rigid body mass, $\mathbf{T}_G$ is the total torque about G, $[J]$ is moment of inertia tensor in the body system

$$[J] = \begin{bmatrix} J_{11} & J_{12} & J_{13} \\ J_{21} & J_{22} & J_{23} \\ J_{31} & J_{32} & J_{33} \end{bmatrix} \tag{15}$$

The elements J_{11}, J_{22} and J_{33} are moments of inertia while the other elements are products of inertia. If the x′, y′ and z′ coordinate axes coincide with the principle axes of the object, products of inertia vanish.

In order to restrict the movement of the object, the mooring chains are connected to the fixed anchor and moving object in the model [27]. In the simulation, three-dimensional dynamics of the mooring chain and the interaction with the tethered moving object are calculated. Interactions between the tethered moving objects and the mooring chains are implemented by data exchange: the mooring chain model supplies tension forces on the moving objects, and the moving objects provide instantaneous locations of the tether points of the mooring chains [28], [29].

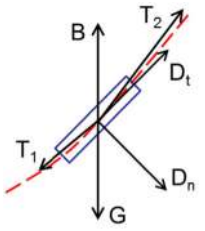

FIGURE 3. A discrete segment of a mooring chain and forces applied on the segment of mooring chain.

A finite segment approach is employed to calculate mooring motion and force. A mooring chain is divided uniformly into a number of discrete cylinder segments with material distribution and uniform diameter. Each chain has its own length, diameter, mass density and physical properties. The computational nodes are located at the segment centers (Fig. 3).

The dynamic equation of motion for each segment is

$$m_s\frac{d\mathbf{v}_s}{dt} = \mathbf{G} + \mathbf{B} + \mathbf{T}_1 + \mathbf{T}_2 + \mathbf{D}_n + \mathbf{D}_t \tag{16}$$

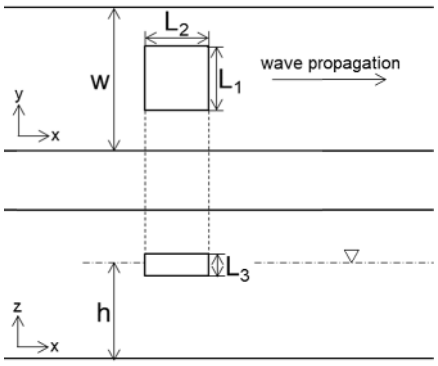

FIGURE 4. Schematic layout of the simulation.

where m_s is mass of a segment, $\mathbf{v}_s$ is the center velocity of the segment, t is the time, **G** is the gravity, **B** is the buoyancy. $\mathbf{T}_1$ and $\mathbf{T}_2$ are the tension forces at the two ends of the segment, $\mathbf{D}_n$ and $\mathbf{D}_t$ are the fluid drag forces in normal and tangential directions of the segment, respectively.

$$\mathbf{D}_n = -C_n \rho_w A_n \mathbf{v}_{r,n} |\mathbf{v}_r| \tag{17}$$

$$\mathbf{D}_t = -C_t \rho_w A_t \mathbf{v}_{r,t} |\mathbf{v}_r| \tag{18}$$

where C_n and C_t are force coefficients in the normal and tangential directions of the segment, respectively. $\mathbf{v}_{r,n}$ and $\mathbf{v}_{r,t}$ are the components of the segment mass center velocity $\mathbf{v}_r$. A_n and A_t are the cross-sectional areas in the normal and tangential directions of the segment, respectively.

III. VALIDATION ON NUMERICAL METHODS

A. MOTION OF A FLOATING PLATE UNDER STOKES WAVES

The primary validation case introduces the floating of a plate under Stokes waves simulated in a straight flume, with corresponding experiments conducted by [30]. The computational layout of the square plate is depicted in Fig. 4. The water depth h is fixed in 0.8m. The wave height H is 0.03m, thus the wave length L is 1.26m with the period T of 0.9s. A square plate is used in the simulation with a density of 0.9g/cm^3. Both the length L_1 and width L_2 of the plate are 0.2m, and the thickness L_3 is 0.045m. In order to avoid the reflection of the wave from the outlet, a long computation domain is selected with the length of 50m, the width of 1.55m and the height of 1.5m. The origin of the x coordinate is established at the left boundary and the origin of the z coordinate is set at the bottom boundary. The mesh consists of 354,213 grids and 45 mesh layers are employed to resolve the wave height region with mesh resolution of 0.66 mm.

With the propagation of the wave, the plate drifts along the wave surface in the horizontal and vertical directions (Fig. 5). The temporal elevation of the plate horizontal displacement is plotted in Fig. 6. The displacement ratio α is the horizontal movement distance of the plate to the thickness L_3. At the time of 25s, a steady movement state has yet to be established and the prediction horizontal trajectory of the plate agrees well with experimental results of [30]. Besides, the average velocity of the plate is about 0.023 m/s which is similar to the velocity in the physical experiment. This model can simulate the motion velocity of the object accurately.

B. WAVE FORCES ON A CYLINDER UNDER A SOLITARY WAVE

To evaluate the computational capability of our model in predicting hydrodynamic forces, the second case introduces a submarine cylinder impacted by a solitary wave, with corresponding experiment performed by [31]. In the case, the pipe diameter D is 0.034 m and the space G between

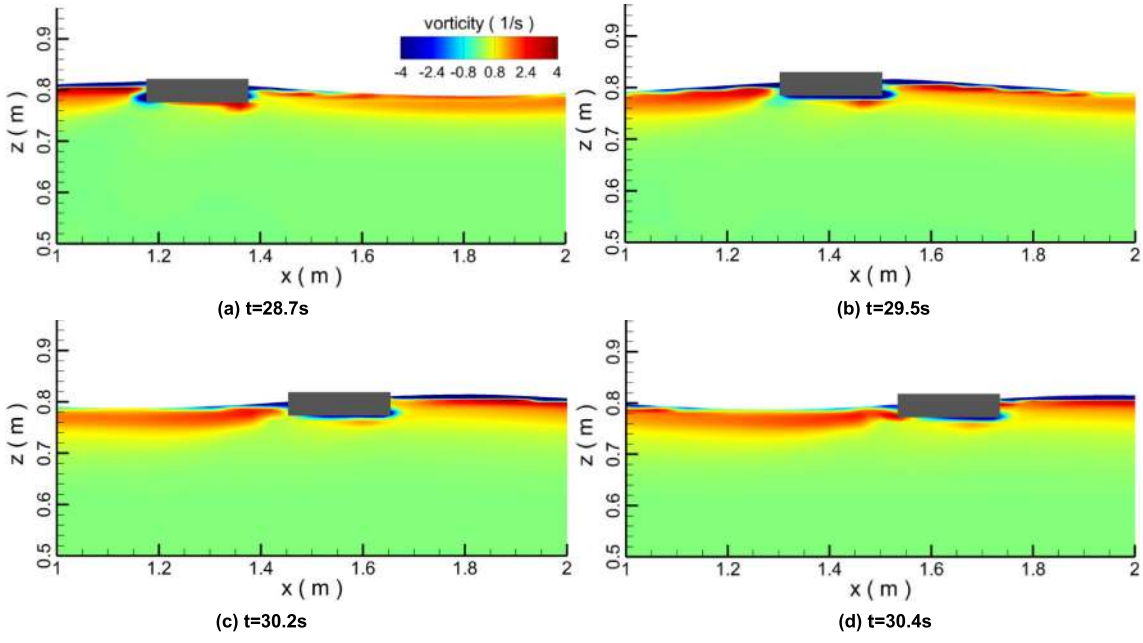

FIGURE 5. The vorticity contour of the plate movement at different time instances.

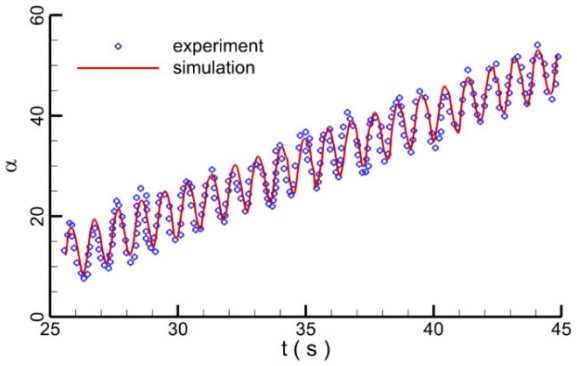

FIGURE 6. The horizontal displacement comparison between the experiment and the simulation.

the pipe and the bottom boundary is 0.0714m. The wave height and water depth are denoted as H of 0.034m and h of 0.17m, respectively. The computational mesh consists of 343,600 elements and the mesh resolution near the circular cylinder is about 0.05mm. To meet the mesh resolution requirement, another two groups of meshes have been generated: a medium and coarse mesh with 174,400 and 89,400 mesh elements, respectively.

Comparisons of time histories of the resultant hydrodynamic forces at the cylinder between measurements and numerical predictions are plotted in Fig. 7, where the forces are normalized by ρghA, namely, $F' = F/\rho ghA$. A is the cross-sectional area of the cylinder ($A = \pi D^2/4$). In the rest of the paper, all the forces are normalized by ρghA. In Fig. 7a, forces for the medium and dense meshes are nearly identical whereas those computed on the coarse mesh are noticeably different from the measurement. Hence, the resolution of dense mesh and medium mesh is sufficient. In order to guarantee the calculation accuracy, in the following simulation, the dense mesh is used depends on the ratio of the moored cylinder diameter to this cylinder diameter of 0.034m. Besides, a temporal convergence is also studied using three different time intervals with $\Delta t_1 = 0.005$s, $\Delta t_2 = 0.01$s and $\Delta t_3 = 0.02$s. Force comparisons with different time intervals are shown in Fig. 7b. When the time interval is 0.005s, the simulation is stable. With the increase of the time interval, the force oscillation begins to occur. When the time interval is 0.01s, the force changes slightly and the solution has become unstable. When the time interval is 0.02s, the solution oscillation is very serious and the simulation results are not in agreement with the experimental results. The accuracy of this solution can not meet the simulation requirement. In general, when the time interval is 0.005s, the simulation is stable and the temporal convergence is very well. The time step of 0.005s used in the numerical model is appropriate, which is also used in all simulation cases. By carrying out the simulation work in this section, the computational capability of our model in predicting the hydrodynamic forces of the cylinder is well verified.

IV. INTERACTION BETWEEN TSUNAMI-LIKE WAVES AND MOODRED CYLINDERS

A. NUMERICAL SETTINGS

In the following sections, hydrodynamic characteristics of the floating cylinder impacted by a tsunami-like wave are systematically investigated, the results of which are compared with the results of the cylinder impacted by a solitary wave. Since the wavelength of a tsunami-like wave is very long, the total length of the computational domain is set as 1500m to avoid wave reflection from the outlet, and the total height of the domain is 20m. The computation domain consists of 405,000 elements. In the zone of the cylinder movement, the cylinder can translate in x and z coordinate of the space system and the spacing mesh resolution is 0.5mm. The computation domain is gradually stretched from the cylinder working zone (150m<x<250m).

In the research, it is hard to solve the fine CFD model with dense mesh of 1.5mm next to moored floating marine cylinder using real-world tsunami wave. So, under the condition that the characteristics of tsunami wave remain unchanged, tsunami-like waves are used in this study depending on the scaling principle. In the simulation, the wave height H and still water depth h are selected as 2.0m and 8.0m, respectively. Correspondingly, the period under the wave height of 2.0m and water depth of 8.0m is much less than under the wave height of 6.7m and water depth of 204.0m. Because the environment conditions are different, the periods

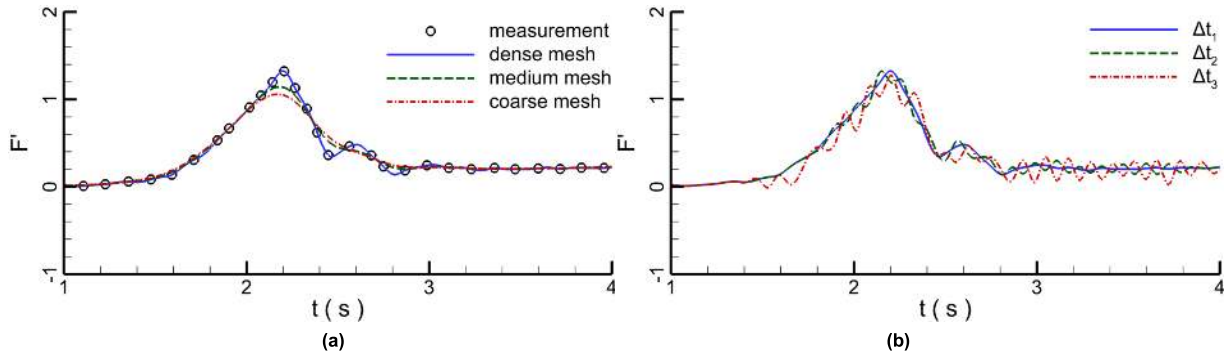

FIGURE 7. Force comparisons; (a) different meshes; (b) different time intervals.

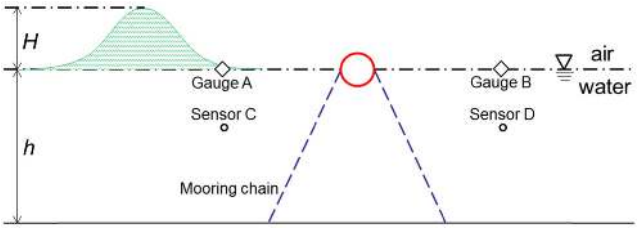

FIGURE 8. Computational layout for wave impacting a single cylinder.

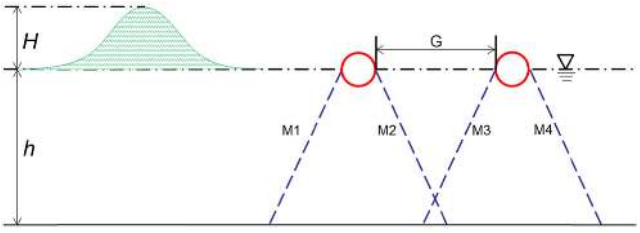

FIGURE 9. Computational layout for wave impacting cylinders in tandem arrangement.

of the tsunami-like waves are also different. The water density is 1000kg/m^3 and the temperature is 20 degrees. The cylinder center is located at (x=205m, z=8m) with density of 500 kg/m^3, and D denotes the diameter of the cylinder which is varies from 0.8m to 1.8m. The free length of the mooring lines is 15m with spring coefficient of 2.4×10^7N per unit length and density of 1125kg/m^3, and each of the mooring lines is divided into 50 segments. The properties of the mooring lines are chosen depending on the criteria [32]. The initial junction locations of the cylinder with the front and rear mooring lines are (x=204.5m and z=8m) and (x=205.5m and z=8m), respectively. The end components of the front and rear mooring lines at the seabed are fixed at (x=200m and z=0m) and (x=210m and z=0m), respectively.

The computational layout of the single cylinder is shown in Fig. 8. In order to analyze if the cylinder has some effects on the progressive wave, the gauges of water elevation are set at the x=50m (gauge A) and 250m (gauge B) for recording the change of the water level. Besides, the velocity sensor C and D are located at the point of (x=50m and z=4.33m) and (x=250m and z=4.33m).

Except for the single cylinder structures, tandem arrangement of offshore cylinder structures is also often seen in the coastal and ocean infrastructures, for instance anchored tandem offshore vessels, aquaculture boxes, components of the semi-submersible drilling platforms and transportation pipelines. To reveal the hydrodynamic characteristics of objects in tandem arrangement subjected to a tsunami-like wave, numerical simulations of the tandem cylinders under tsunami waves are also conducted and compared to the single cylinder cases. The computational layout for the cylinders in tandem arrangement is shown in Fig. 9, where G is the distance between two cylinders. S is the ratio of the distance G to the cylinder diameter D. The mooring chains M1 and M2 connect the upstream pipeline, and M3 and M4 connect the downstream pipeline.

B. COMPARISON OF HYDRODYNAMIC CHARACTERISTICS BETWEEN TSUNAMI-LIKE WAVE AND SOLITARY WAVE

In order to fully understand the differences between the tsunami-like wave and solitary wave, the effects of both waves on the single floating cylinder are analyzed systematically in four aspects as follows:

1) WAVE ELEVATION AND VELOCITY

The profiles of the tsunami-like wave and the solitary wave recorded in two water level gauges are displayed in Fig. 10. For peak comparison between the solitary wave and the tsunami-like wave, the water elevation of the solitary wave has been shifted to 113.5s to coincide with that of the tsunami-like wave. When the waves propagate in the channel without the moored cylinders, the water level recorded in gauge B (Fig. 10a) is unchanged. However, when the waves pass through the cylinder, the peak elevations of the solitary wave and the tsunami-like wave recorded at the rear sensor decrease in 3.8% and 1.7% respectively compared with those recorded at the front side of the cylinder (Fig. 10b). Besides, due to the effect of the cylinder fluctuation, the waves have changed slightly.

The wave velocities of both waves in x-direction and z-direction at points of C and D are recorded by velocity sensors. When both waves are not disturbed by the cylinder (Fig. 11a and b), the maximum horizontal velocities of the tsunami-like wave and solitary waves recorded at sensor C are about 2.07m/s and 2.01 m/s respectively, which are much larger than the maximum vertical velocities of 0.235 m/s and 0.288 m/s. The maximum horizontal velocity of the tsunami-like wave is more than that of the solitary wave, however, the vertical velocity of the tsunami-like wave is less than the solitary wave. When the waves pass through the floating cylinder, the wave velocities are affected by the moving cylinder (Fig. 11c and d). The maximum horizontal velocities of the tsunami-like wave and the solitary wave recorded at sensor D are about 2.063 m/s and 1.98 m/s, and the maximum vertical velocities are about 0.209 m/s and 0.267 m/s, respectively. Besides, as can be seen in Fig. 11b and d, the vertical velocity of the solitary wave is more than that of the tsunami-like wave. The velocity magnitudes of the tsunami-like wave and the solitary wave are shown in Fig. 12. In total, the maximum velocity magnitude of the tsunami-like wave is more than that of the solitary wave.

2) FLOW FIELD

When the waves pass through the floating cylinder, the vorticity contours are shown in Fig. 13 and 14 for the solitary wave and the tsunami-like wave. When the solitary wave enters the computational domain, the flow is stationary at the initial stage and the floating cylinder does not move, as shown

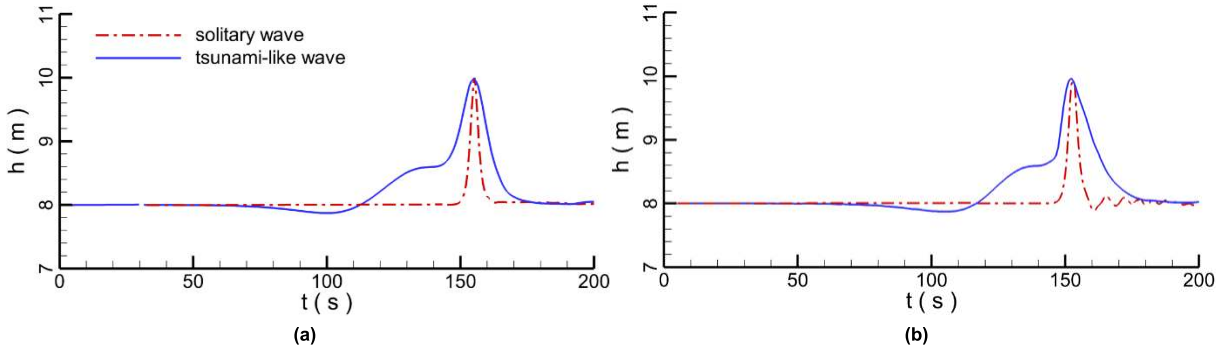

FIGURE 10. Comparison of water elevations of solitary wave and tsunami-like wave; (a) without the cylinder (2) under the effect of the cylinder.

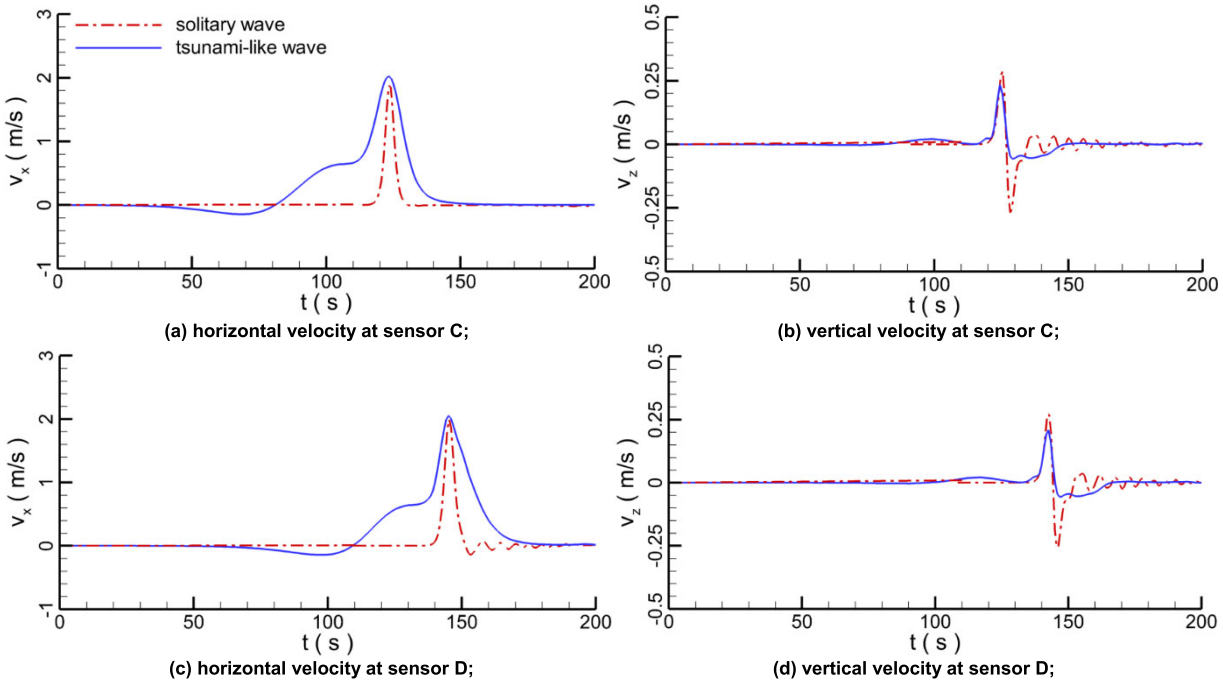

FIGURE 11. Both horizontal and vertical velocities at two sensors.

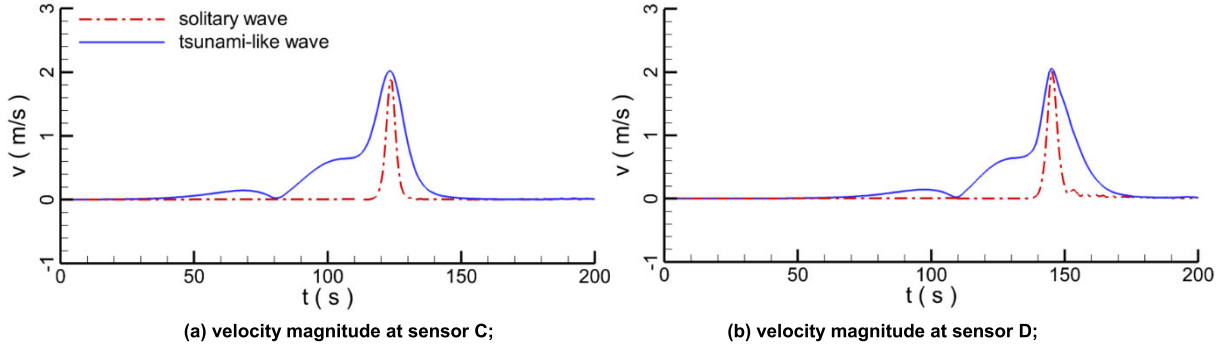

FIGURE 12. Velocity magnitude in sensor C and sensor D.

in Fig. 13a. As the solitary wave approaches the cylinder, the cylinder moves upward and backward with the increase of the water elevation (Fig. 13b and c). When the solitary wave passes the cylinder, due to the traction of the mooring lines, the cylinder moves to the equilibrium position and a detached vortex is gradually generated, as shown in Fig. 13d and e.

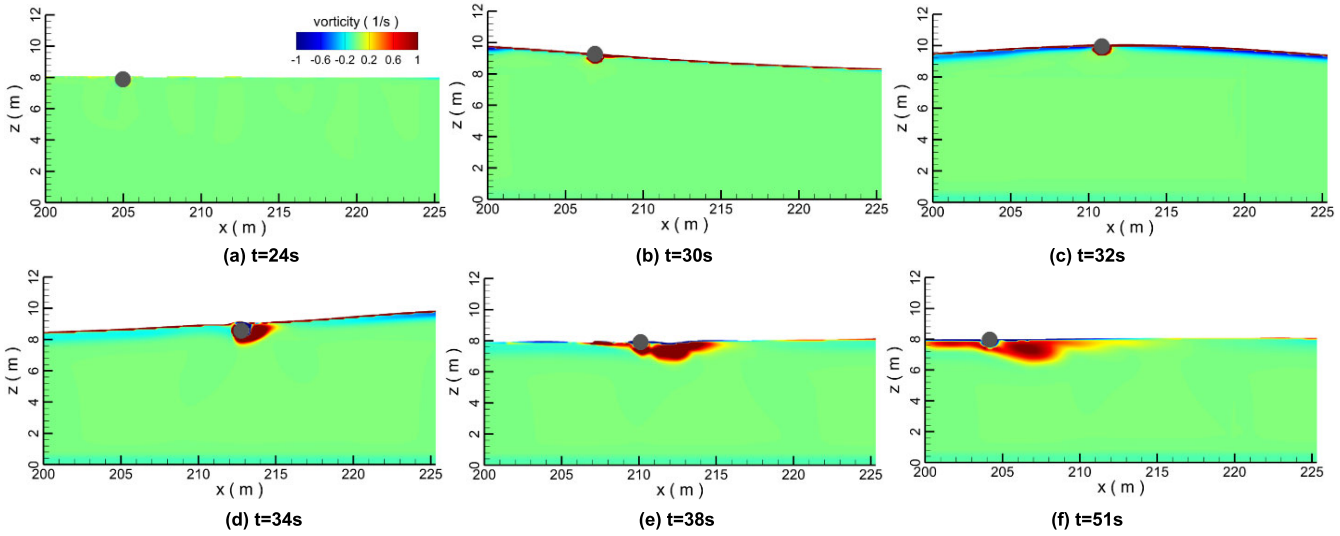

FIGURE 13. The flow fields at different times under the solitary wave.

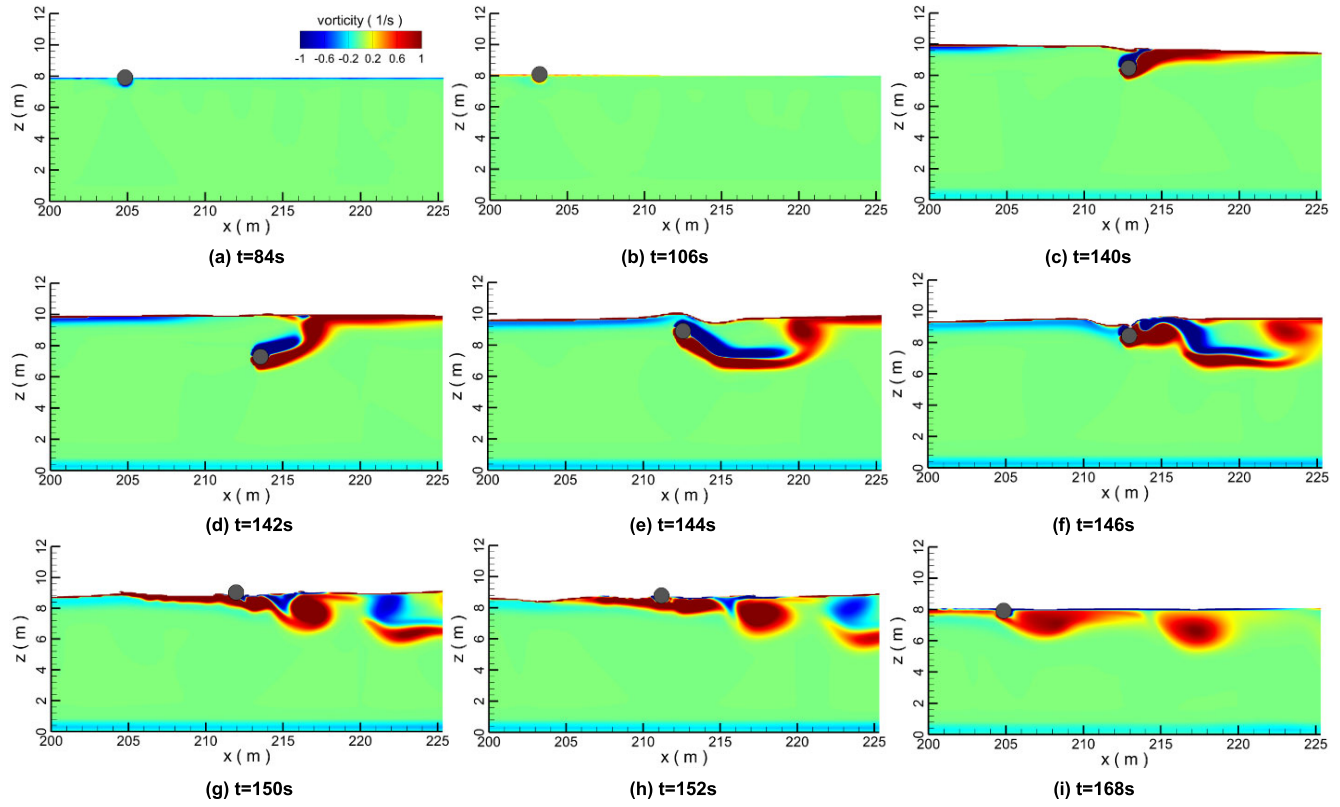

FIGURE 14. The vorticity contours of flow field at different times under the tsunami-like wave.

After the solitary wave moves past the cylinder, a big vortex appears due to the relative movement between the wave and cylinder (Fig. 13f).

As for the tsunami-like wave impinging the cylinder, the snapshots of vorticity and velocity contours are plotted in Figs. 14 and 15. When the depression wave portion of the tsunami-like wave propagates in the computational domain, the water elevation decreases, which induces the cylinder moves to the upstream. Due to the flow is rather weak, the velocity is very small in the flow field and the cylinder moves lightly. As the wave continues to travel, the flow velocity increases inducing the cylinder drifts to the downstream. The cylinder is moored by the chain, the free length of which is 15m. When the cylinder moves from upstream

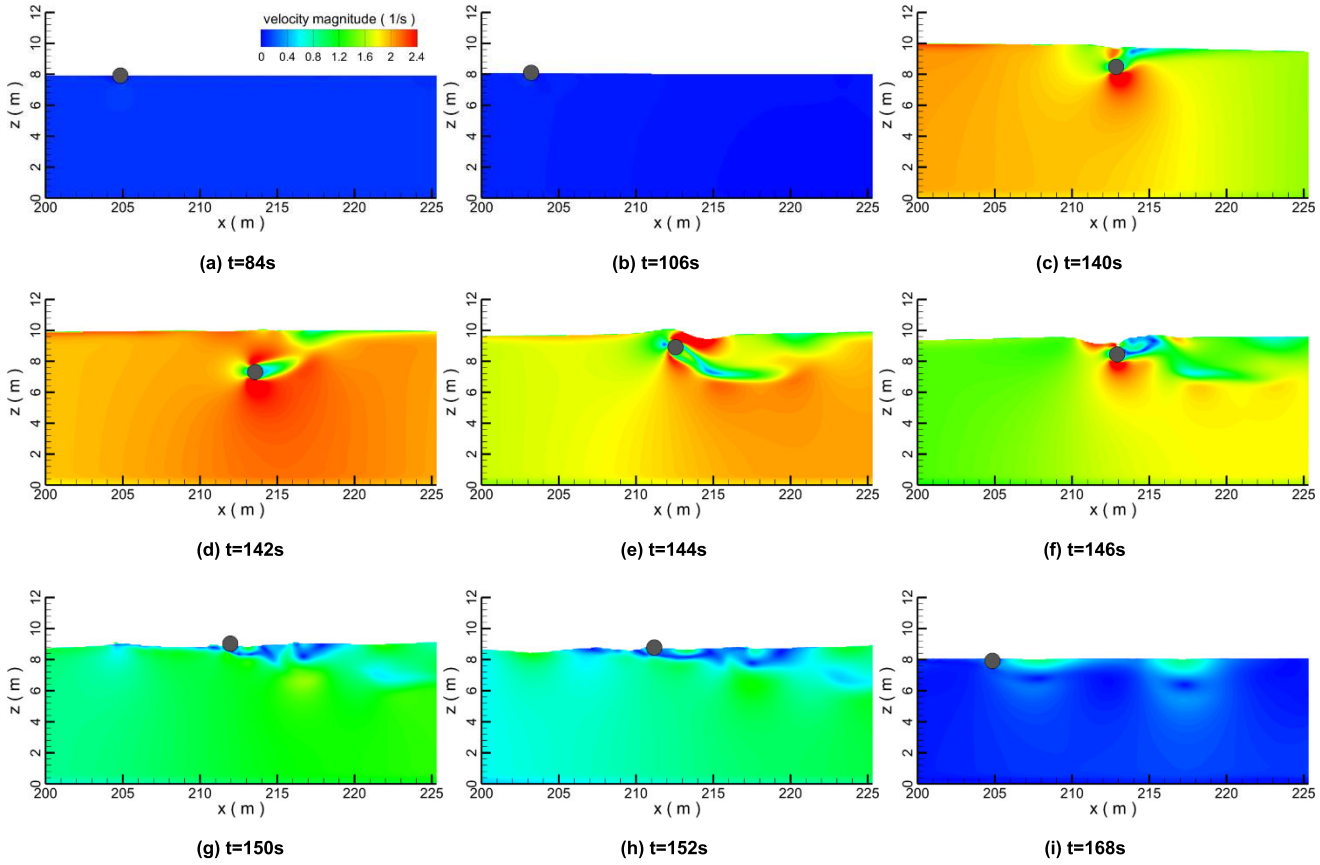

FIGURE 15. The velocity contours of flow field at different times under the tsunami-like wave.

to downstream under the tsunami-like wave and the distance between the moving cylinder and the fixing point of the mooring line is larger than 15m, the movement of the cylinder which suffers the wave forces and the traction forces is under the effects of the wave and the mooring chains. The cylinder oscillates dramatically and bobs up and down on the water when the secondary elevated wave portion of the tsunami-like wave reaches the cylinder. At this time, the flow velocity around the cylinders reaches the maximum and several vortices shake and shed behind the moving cylinder. When the wave passes over the cylinder, the flow velocity and forces on the cylinder reduces, and the cylinder restores to the initial potion due to the traction force of the mooring chain. In the movement, the vortices shed from the cylinder, which induces the fluctuation of the cylinder.

Through the comparison between both waves, the vibration intensity of the cylinder under the tsunami-like wave is more than that under the solitary wave. There are three main reasons for the interesting phenomena: firstly, the velocity magnitude of the tsunami-like wave is more than that of the solitary wave; secondly, before the secondary elevated wave of tsunami-like wave impinges on the cylinder, the depression and preceding wave portions of the tsunami-like wave have caused the vibration of the cylinder, and the secondary elevated wave enhances the amplitude of vibration. Compared with the solitary wave, both the duration and the wave length of the tsunami-like wave are much longer, which induces the forces and the movement of the cylinder under the tsunami-like wave are more serious than that under the solitary wave.

3) CYLINDER MOVING TRAJECTORY AND VELOCITY

The cylinder moving trajectories in the horizontal and vertical directions under the tsunami-like wave and the solitary wave are depicted in Fig. 16. With the propagation of the wave, the cylinder moves downstream and the displacement of the cylinder also changes with the change of the water elevation. After the wave passes the cylinder, the cylinder moves to the equilibrium position due to the traction of the mooring lines. However, because of the inertial force of the object, the cylinder moves upstream over the initial equilibrium position at the time of 170s. After long time damping of the cylinder movement, the cylinder stays in equilibrium at time of 450s for the tsunami-like wave and 350s for the solitary wave.

In the horizontal direction, the maximum displacement coordinate of the cylinder under the tsunami-wave is 213.606m, larger than the displacement under the solitary wave which is 212.82m. The minimum displacement coordinates of the two waves are both at 196.8m approximately.

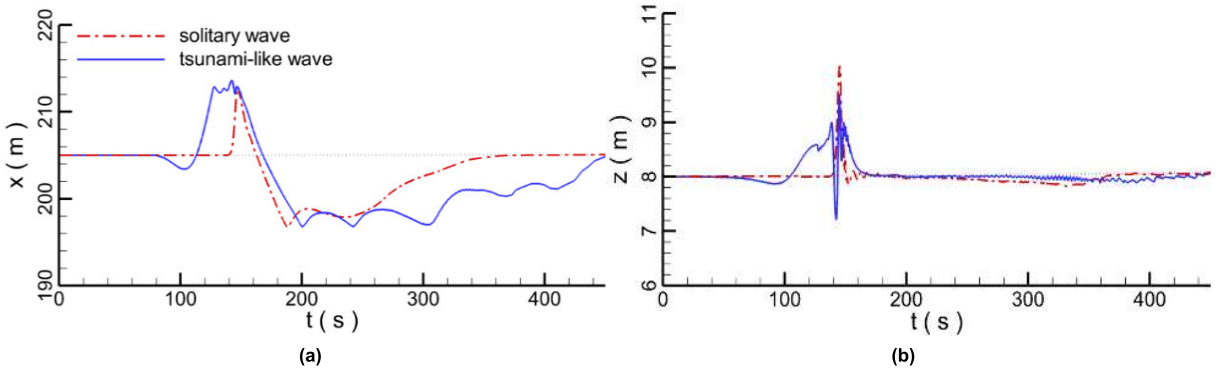

FIGURE 16. Cylinder moving trajectories under both waves; (a) horizontal displacement; (b) vertical displacement.

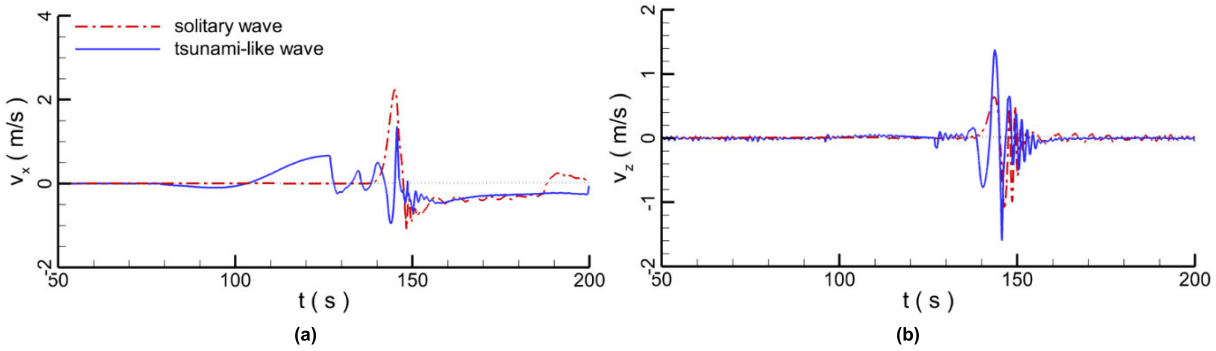

FIGURE 17. Velocities of the cylinder under the tsunami-like wave and the solitary wave; (a) horizontal velocity; (b) vertical velocity.

The horizontal offset ranges of the cylinder under tsunami-like wave and solitary wave are 16.806m and 16.02m, respectively. In the vertical direction, as the wave level changes, the cylinder moves at the water surface for the solitary wave. Nevertheless, when the secondary elevated wave portion of the tsunami-like wave reaches the cylinder, the cylinder vibrates violently up and down in the water. The maximum and minimum vertical coordinates of the cylinder are 9.51m and 7.21m under the tsunami-like wave, and 10.032m and 7.87m under the solitary wave, respectively. The vertical offset ranges of the cylinder under tsunami-like wave and solitary wave are 2.30m and 2.162m, respectively. It is found that although the moving states of the cylinder are completely different under the tsunami-like wave and solitary wave, the cylinder moving ranges are similar to each other, because the maximum movement distance of the cylinder is limited by the free length of the mooring chain.

The velocity comparison between the tsunami-like wave and the solitary wave is plotted in Fig. 17. The maximum horizontal and vertical velocities of the cylinder under the solitary wave are 2.23m/s and 0.64m/s, and both the maximum velocities under the tsunami-like wave are 1.36m/s and 1.38m/s, respectively. When the peak of the tsunami-like wave arrives at the cylinder, the cylinder submerges in the water. As a result, the horizontal velocity of the cylinder under the tsunami-like wave is smaller than that of the solitary wave,

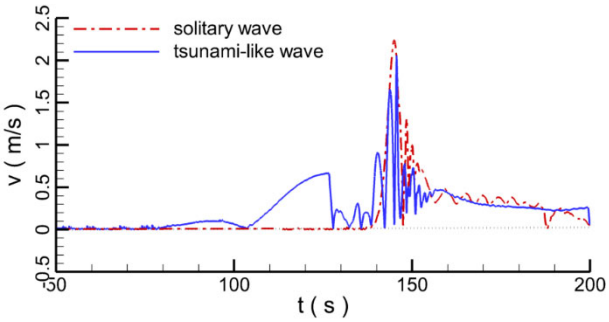

FIGURE 18. Velocity magnitude of the cylinder under the tsunami-like wave and the solitary wave.

but the vertical velocity magnitude of the cylinder under the tsunami-like wave is larger. Besides, the velocity of the cylinder decays periodically due to the damping function between the cylinder and the water, which is more obvious in the vertical velocity under the tsunami-like wave. Although the horizontal velocity of the cylinder under the solitary wave is more than that under the tsunami-like wave, the total velocity magnitudes of both waves are similar to each other, as shown in Fig. 18. The oscillation frequency of velocity under the tsunami-like wave is larger than that under the solitary wave, which might be one of the dominating reasons for structural failure damage.

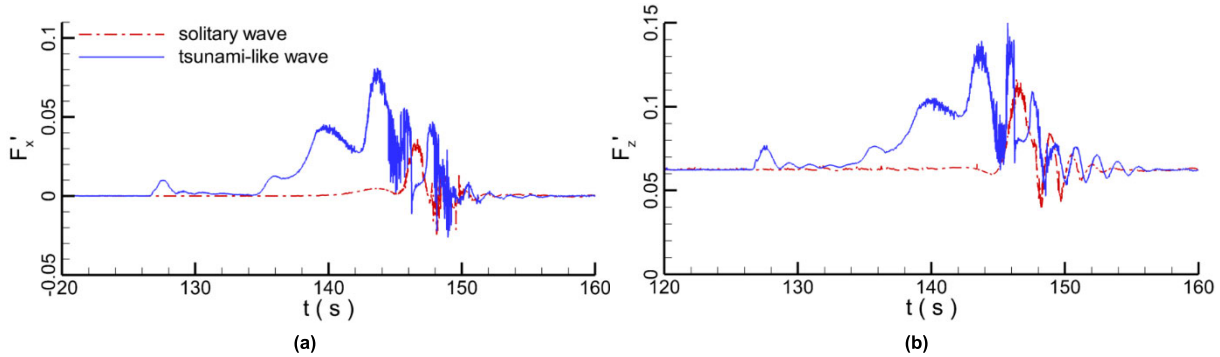

FIGURE 19. Forces on the cylinder under the tsunami-like wave and the solitary wave; (a) horizontal force; (b) vertical force.

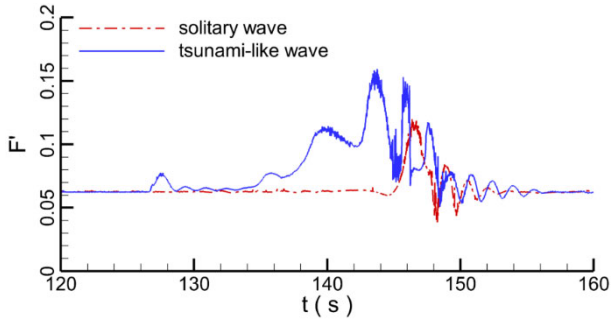

FIGURE 20. Force magnitudes on the cylinder under the tsunami-like wave and the solitary wave.

4) FORCES ON THE CYLINDER AND MOORING CHAIN

The horizontal and vertical forces on the cylinder under both waves are drawn in Fig. 19. Both the horizontal and vertical forces on the cylinder under the tsunami-like wave are more than those under the solitary wave. The active duration of the force on the cylinder under the tsunami-like wave is also more than that under the solitary wave in both different direction forces.

The comparison between the total force magnitudes on the cylinders under the tsunami-like wave and the solitary wave is displayed in Fig. 20. Because the depression wave portion of the tsunami-like wave can only generate a small velocity, the force during the depression wave stage is unnoticeable. With the increase of the water surface, the current velocity around the cylinder site increases and the force gradually increases as well. The temporal evolution of the force under the tsunami-like wave shares a similar pattern to the tsunami-like wave itself before the secondary elevated wave, but with severe oscillations during the secondary elevated wave due to the relative body motion of the cylinder. The maximum force under the tsunami-like wave is about 1.5 times of that under the solitary wave and the duration under the tsunami-like wave is longer, which demonstrates the underlying reasons for the devastatingly destructive power of tsunami wave for its high energy with a long period.

When the wave causes motions of the cylinder, the motion range of the cylinder is restricted by the upstream and downstream mooring lines. Since the mooring chains cannot withstand compression, the tension forces of both mooring lines are more than zero (Fig. 21), in which F_{mf}' and F_{mb}' denote the tension force of the upstream mooring line and the downstream mooring line respectively. When the cylinder moves, the tension forces change with the forces on the cylinder because of the interaction between the cylinder and the mooring lines. The tension force of the upstream mooring line is much more than that of the downstream mooring line because when the wave passes through the cylinder, the upstream mooring line plays a dominating restriction role on the cylinder movement from upstream to downstream. When the cylinder restores to the equilibrium state, the downstream mooring chain plays an important role on the stability of the cylinder. Depending on the tension force comparison of mooring line under the tsunami-like wave and the solitary wave, it is found that the tension forces of both mooring lines under the tsunami-like wave are more than that under the solitary wave. The tension forces of the upstream and downstream mooring lines under the tsunami-like wave are about 1.8 and 1.5 times of those under the solitary wave, respectively.

In the comparison of hydrodynamic characteristics between the solitary and tsunami-like wave, there are some oscillations of cylinder moving trajectories, velocities, and the forces of cylinder and mooring chain, which are caused by two main reasons. On the one hand, there are some unstable numerical solutions due to the interpolations made between the base mesh and the object. In the model, the immersed boundary (IB) method is used and the object is embedded in the mesh. The motion of object in the mesh may induce the poor iteration convergence which also exits in every interpolation of dynamic mesh computation in computational fluid dynamics (CFD). However, compared with other interpolation schemes, the IB method is developed specially to reduce the effects of the moving object on the interpolation scheme. Although some numerical instability exits, it will not have a substantial impact on the calculation results. On the other hand, as the tsunami-like wave propagates, the cylinder oscillates dramatically when the secondary elevated wave portion of the tsunami-like wave reaches it and the cylinder

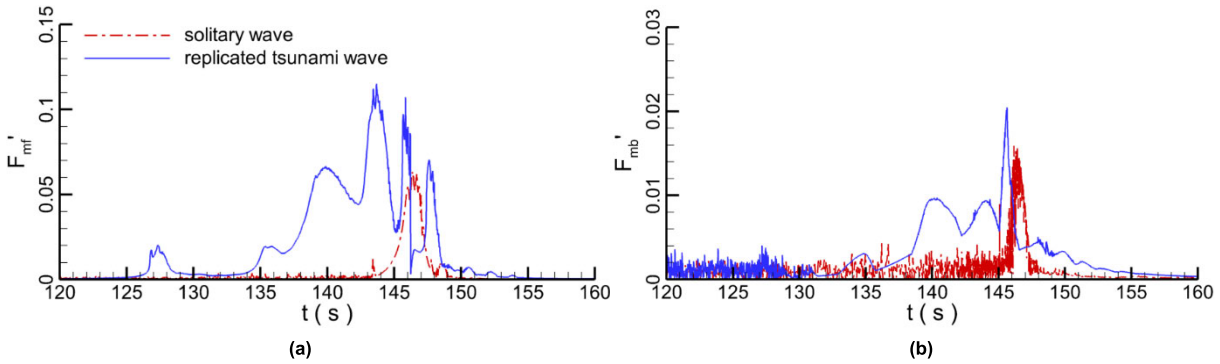

FIGURE 21. Tension forces of mooring lines under the tsunami-like wave and the solitary wave; (a) upstream cylinder; (b) downstream cylinder.

TABLE 1. Comparison indices between the tsunami-like wave and solitary wave.

			Tsunami-like wave	Solitary wave
Wave	Height attenuation		1.7 %	3.8 %
	Maximum velocity (m/s)	Horizontal	2.07	2.01
		Vertical	0.235	0.288
		Magnitude	2.083	2.030
Cylinder	Maximum offset range (m)	Horizontal	16.806	16.02
		Vertical	2.30	2.162
	Maximum velocity (m/s)	Horizontal	1.36	2.23
		Vertical	1.38	0.64
		Magnitude	1.938	2.320
	Force	Horizontal	0.081	0.0398
		Vertical	0.1526	0.1162
		Magnitude	0.1592	0.1206
Mooring chain	Tension force	Upstream	0.1152	0.0636
		Downstream	0.0205	0.0159

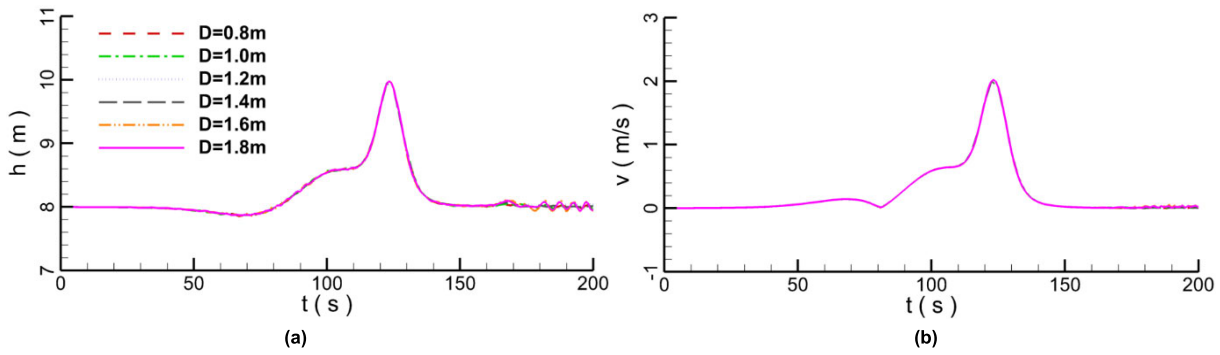

FIGURE 22. The initial water elevations and velocities; (a) water elevation recorded at gauge A; (b) velocity magnitude recorded at sensor C.

bobs up and down on the water. Compared with the tsunami-like wave, the oscillation factors (e.g. trajectory, velocity and force) under the solitary wave is weaker inducing the wave form has a great impact on the moored floating cylinders. In general, the numerical instability and the intensity of the wave cause the oscillations of cylinder motion trajectory, velocity and forces and the latter plays a leading role.

Summary of comparison indices between the tsunami-like wave and solitary wave are listed in Table 1. Overall, compared with the solitary wave, the wave profile of the tsunami-like wave includes three wave portions. The period, wave length and wave velocity magnitude of the tsunami-like wave are all more than that of the solitary wave. When the wave passes through the floating cylinder, both the wave height and

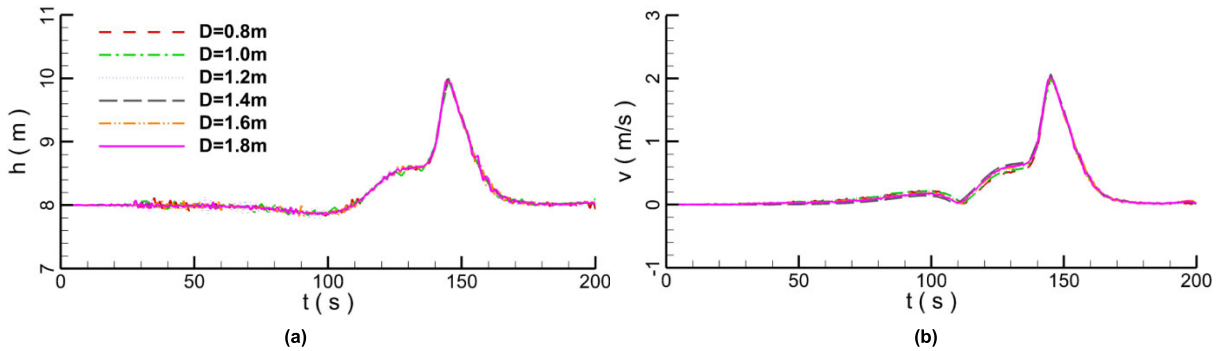

FIGURE 23. The water elevations and velocities; (a) water elevation recorded at gauge B; (b) velocity magnitude recorded at sensor D.

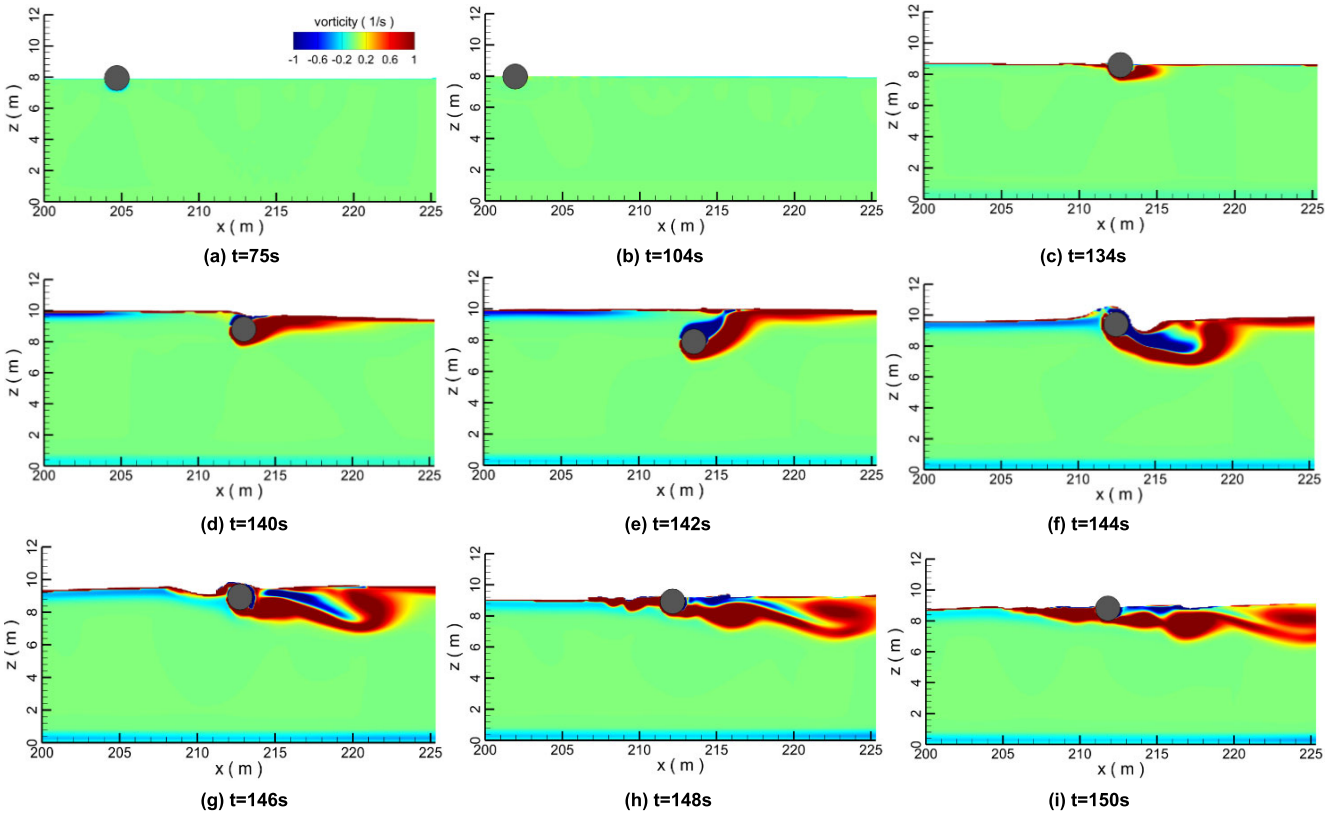

FIGURE 24. Snapshots of vorticity contour at different time instances with D=1.6m.

wave velocity magnitude are attenuated due to the motion of cylinder. However, the wave height reduction rate after the tsunami-like wave passing the cylinder is less than that of the solitary wave. When the cylinder moves in the wave, the maximum displacement of the cylinders under the tsunami-like wave and the solitary wave are close because of the restriction of the mooring chains. After the wave passes through the cylinder site, according to the damping interaction between the object and water, the cylinder gradually restored to the initial equilibrium position. Due to the cylinder absorbs more wave energy under tsunami-like wave than that under solitary wave, the dissipation of the energy under tsunami-like wave takes more time and the recovery duration is much longer. Moreover, compared with the solitary wave, the forces of the cylinder caused by tsunami-like wave are larger with much longer durations, too. Correspondingly, the tension forces of the mooring chains are also much larger than that under the solitary wave.

C. TSUNAMI-LIKE WAVE ON SINGLE CYLINDERS

In the ocean, there are many floating bodies with different sizes. In order to reveal the hydrodynamic characteristics of the different objects under the tsunami wave, in this section, the effects of the tsunami-like wave on the floating cylinders

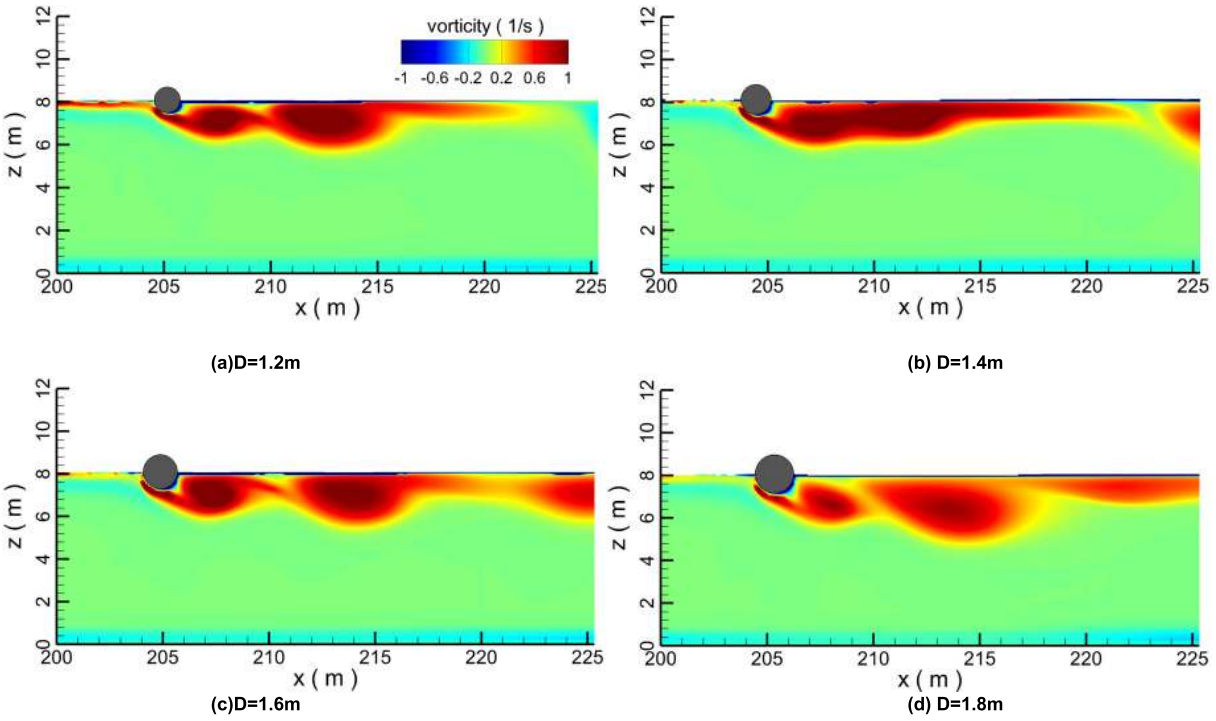

FIGURE 25. Vorticity contours with different cylinder diameters.

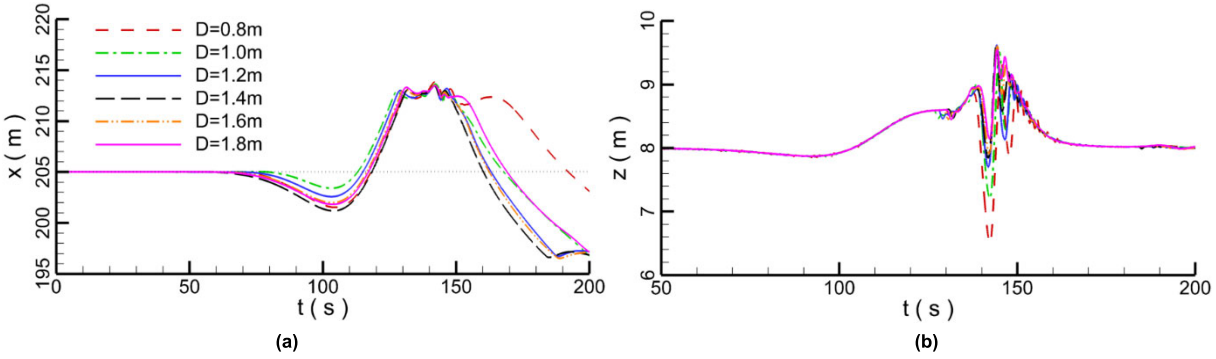

FIGURE 26. Cylinder moving trajectories with different diameter cylinders; (a) horizontal displacement; (b) vertical displacement.

with different diameters are investigated. The cylinder diameter is set as 0.8m, 1.0m, 1.2m, 1.4m, 1.6m, and 1.8m, respectively. The hydrodynamic environment is the same to that in section 4.1. The still water depth is 8m, and the wave height is 2m.

The initial water elevations and velocities of the tsunami-like wave generated in the wave boundary are the same, as shown in Fig. 22. When the tsunami-like wave passes through the cylinder, both water surfaces and velocities oscillate due to the disturbance of the movement of the cylinder, and the waveforms have also changed (Fig. 23). However, the effects of the cylinder diameter on the tsunami-like wave elevation are not significant since the cylinder diameter is much smaller compared to the tsunami wave length and water level.

When the tsunami-like wave approaches the floating cylinder, the water flow shed contours are shown in Fig. 24. In the figure, the cylinder diameter is 1.6m. At the initial time, the cylinder stands still on the water surface (Fig. 24a). Thereafter, the cylinder moves upstream due to the decrease of the water elevation at the depression wave portion of the tsunami-like wave, as shown in Fig. 24b. When the preceding wave portion of the tsunami-like wave reaches the cylinder, the cylinder moves downstream and rises with the increase of the water elevation, besides, there is a detached vortex behind the cylinder (Fig. 24c). When the water elevation approaches the maximum at the secondary elevated wave portion of the tsunami-like wave, the cylinder suffers from the hydrodynamic forces and the tension forces of the mooring chains, then oscillates around the water surface. At the time

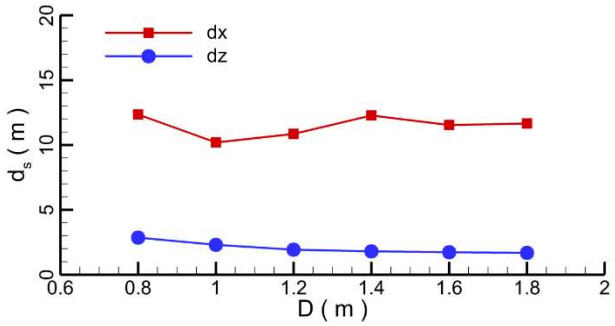

FIGURE 27. The movement offset of the cylinders with different diameters.

of 144s in Fig. 24f, the cylinder floats out of the wave surface. The water flow is blocked by the cylinder and the water elevation difference before and after the cylinder is very obvious. Furthermore, a pair of the large detached vortices is generated behind the cylinder and sheds with the movement of the cylinder. After the wave passes through cylinder, the water level decreases and the cylinder moves to the initial equilibrium position according to the drag of the mooring chain, while a series of vortices shed from the cylinder afterwards. When the cylinder arrives at the equilibrium position, Fig. 25 displays the snapshots of vorticity contours with different cylinder diameters. With the increase of the cylinder diameter, the vortex shed from the cylinder becomes bigger and bigger.

The moving trajectories of the different cylinders are recorded in the x-direction and z-direction, which are similar to each other as shown in Fig. 26. Affected by the secondary elevated wave, the displacement of the cylinder in the horizontal direction has reached the maximum and the cylinder vibrates violently up and down. When the cylinder diameter is 0.8m, the residence time of the cylinder at the maximum displacement is the longest and the sinking depth reaches maximum.

Fig. 27 depicts the maximum movement offsets (ds) of cylinders with different cylinder diameters in the horizontal and vertical directions. When the cylinder diameter is 0.8m, both the horizontal and vertical movement offsets of cylinder are larger than other cylinders. Because when the cylinder diameter is small, the weight of the cylinder is light, which causes the object inertia becoming weak. This cylinder is vulnerable to the hydrodynamic forces, and under the tsunami-like wave, the cylinder with a diameter of 0.8m moves in the largest range. When the cylinder diameter is larger than 1.0m, the horizontal movement offsets of different cylinders are similar to each other. The horizontal movement offsets of all cylinder are between 10.21m and 12.31m. In the vertical direction, the movement offsets of the cylinders are much less than that in the horizontal direction due to the effect of the wave height and the mooring line dragging. With the increase of the cylinder diameter, the vertical movement offset of the cylinder decreases gradually, which indicates the smaller the cylinder, the more serious the wave effect. The vertical movement offsets of cylinders change from 1.68m to 2.85m. Depending on the comparisons of vertical offsets, it demonstrates that the motion state of different cylinders under the same wave is different. With the increase of the

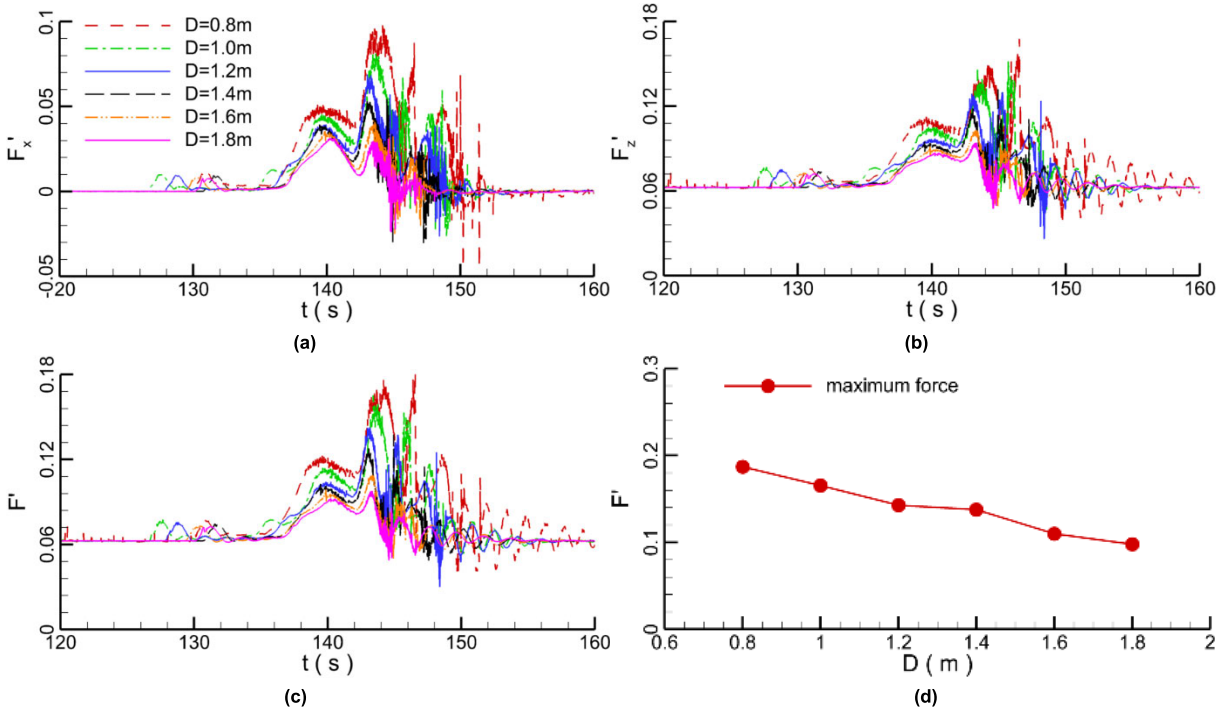

FIGURE 28. The forces on the cylinders with different diameters; (a) horizontal force; (b) vertical force; (c) force magnitude; (d) the maximum force.

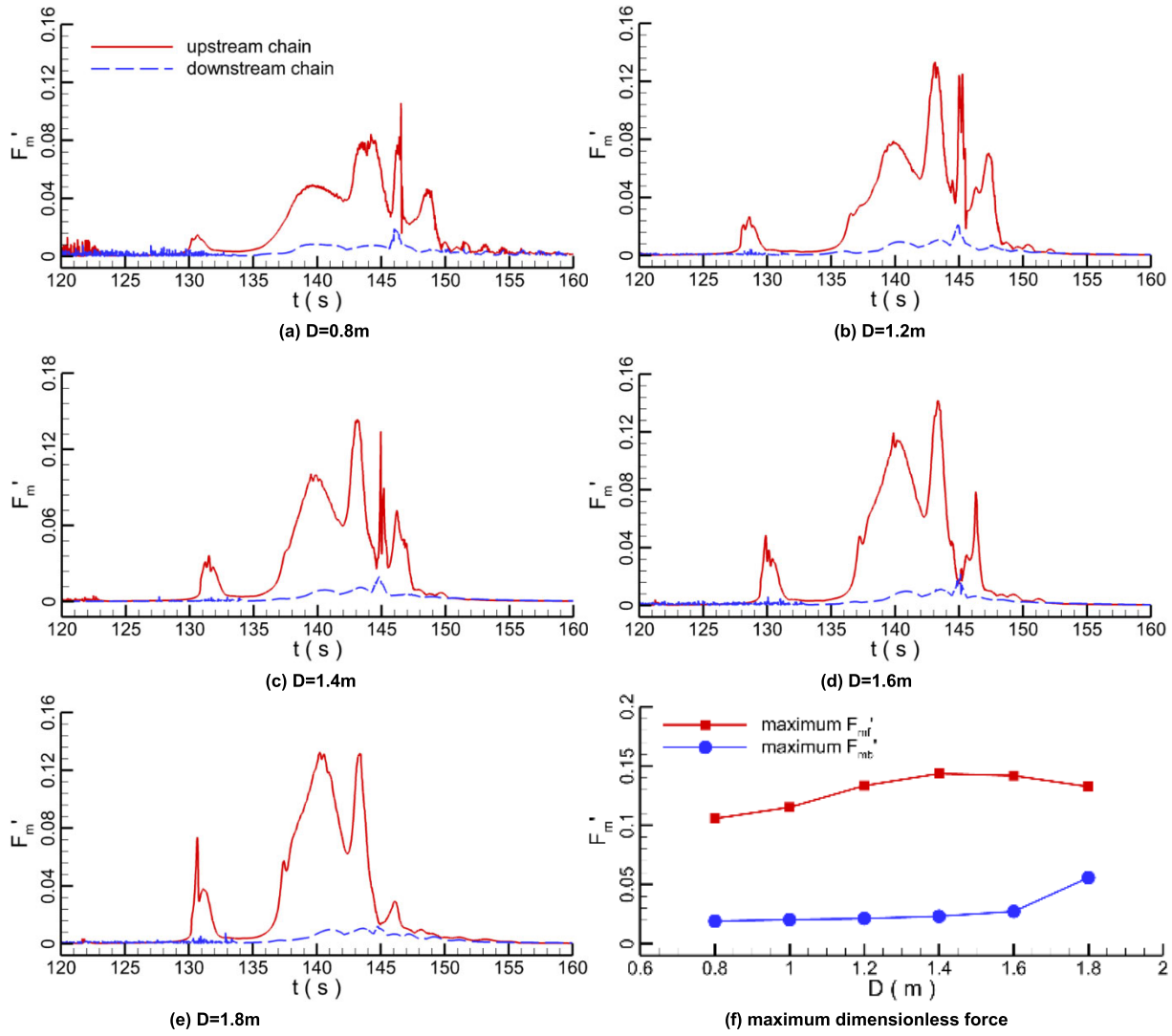

FIGURE 29. Tension forces of mooring chains at different cylinder diameter.

diameter, the movement range of the cylinder decreases. The small objects move more intensely and are liable to break. However, the movement ranges of different cylinders are not very different because the different marine structures nearly suffer from the similar hydrodynamic loads under the tsunami wave and the cylinders are restricted by mooring chains.

The forces on the cylinder change with the cylinder diameter greatly, shown in Fig. 28. Before the secondary elevated wave approaches the cylinder, both the horizontal and vertical forces on the cylinder increase. Affected by the secondary elevated wave, the cylinder oscillates around the water surface and the forces of the cylinders also vibrate strongly. Owing to reason that the forces on the cylinder are nondimensionalized by hydrostatic pressure (ρghA), the effect of the cylinder diameter on the hydrostatic pressure is neglected. With the increase of the cylinder diameter, the horizontal force, vertical force and force magnitude on the cylinder decrease

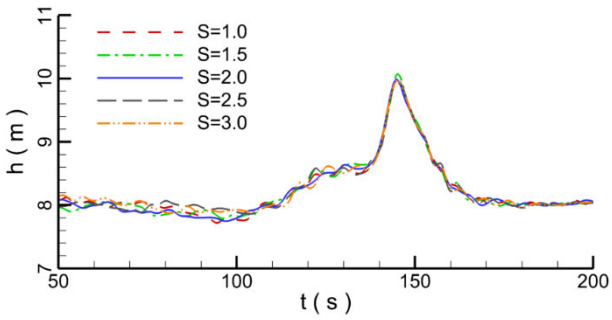

FIGURE 30. Water surface recorded at gauge B.

(Fig. 28c and d), proving that the smaller the diameter is, the more susceptible the cylinder is to the wave.

When the cylinder moves in the water, the cylinder is constrained by the mooring chains. Fig. 29 displays the tension forces of the mooring chains. When the cylinder is subjected

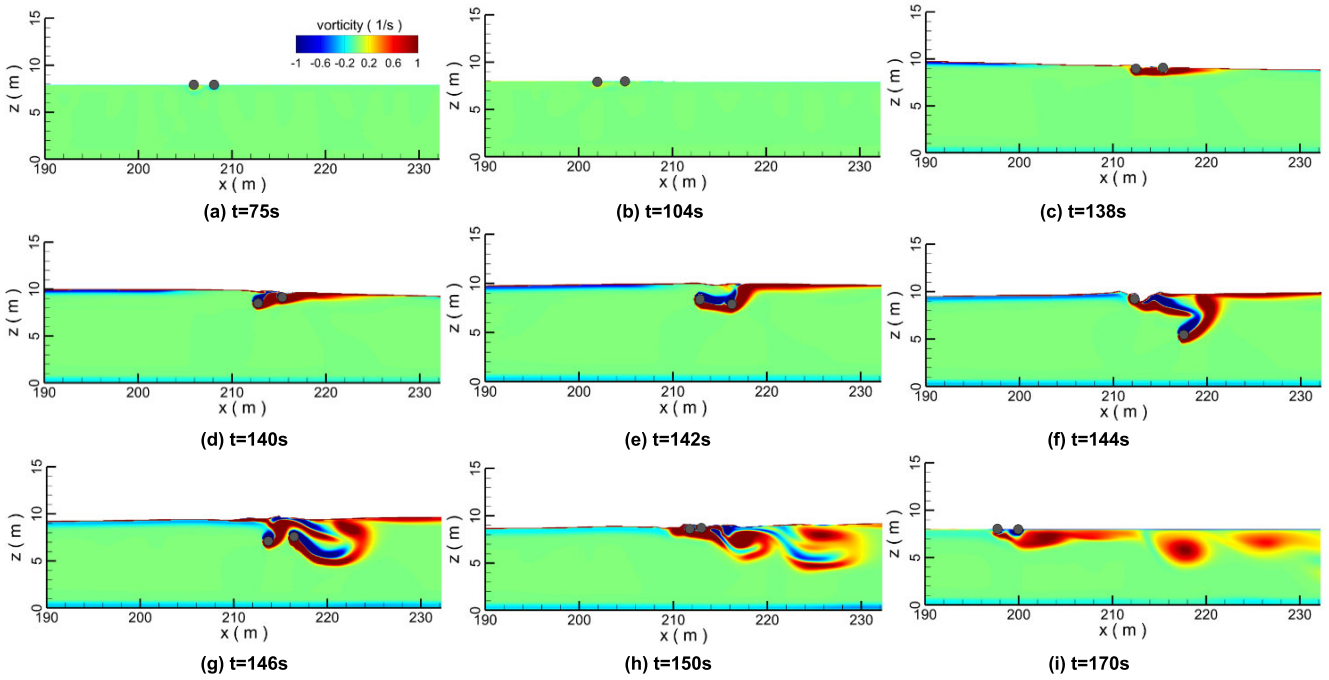

FIGURE 31. Vorticity contours around the tandem cylinder at different times with S=2.0.

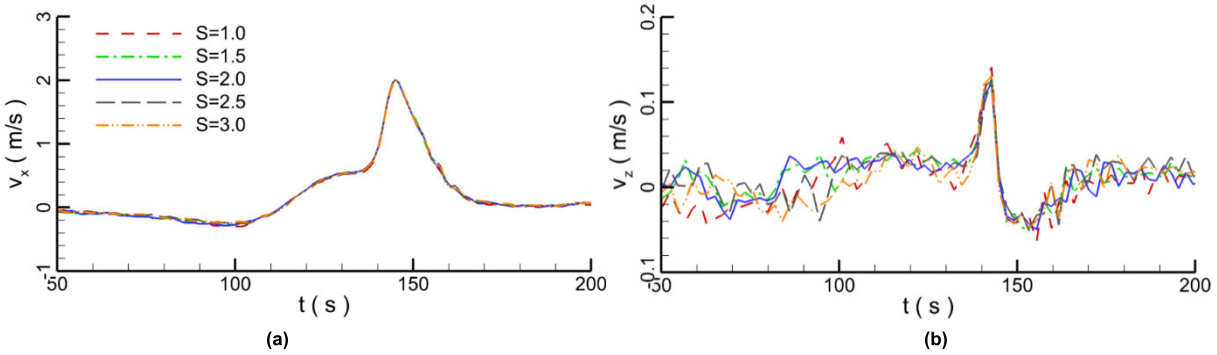

FIGURE 32. Velocity recorded at sensor D. (a) Horizontal velocity. (b) Vertical velocity.

to the wave force, the cylinder drifts downstream and the upstream mooring chain restricts the movement of the cylinder. When the cylinder moves to the equilibrium position, the downstream mooring chain controls the movement of the cylinder. As a result, the tension force of the upstream mooring chain increases with the propagation of the tsunami-like wave, which is much larger than that of the downstream mooring chain. With the increase of the cylinder diameter, the maximum tension force of the upstream cylinder first increases and then decreases when the cylinder diameter exceeds 1.4m, while the maximum force of the downstream cylinder increases monotonously, shown in Fig. 29 (f).

D. TSUNAMI-LIKE WAVE ON TANDEM CYLINDERS

Since tandem object is a commonly used type of offshore structures, in order to improve the understanding of the interaction between the marine structures and tsunami-like wave, the influence of the tsunami-like wave on tandem cylinder is discussed in this section. For tandem cylinders, cylinder spacing is usually considered as the dominate parameter on the hydrodynamic characteristics besides the cylinder diameter, Therefore, five cylinder spacing ratios S of distance between two cylinders G to the pipeline diameter D are selected as $S = 1.0, 1.5, 2.0, 2.5$, and 3.0 in this section to investigate the effects of the dominate parameter.

Fig. 31 depicts the snapshots of the water flow shed with vorticity contours at different time instances at the ratio $S = 2.0$. At the initial stage, the tandem cylinder is still on the water surface (Fig. 31a). After a long time, the depression wave approaches the cylinder. The water surface begins to decrease which indicates the tandem cylinder moves upstream, as shown in Fig. 31b. Water elevation

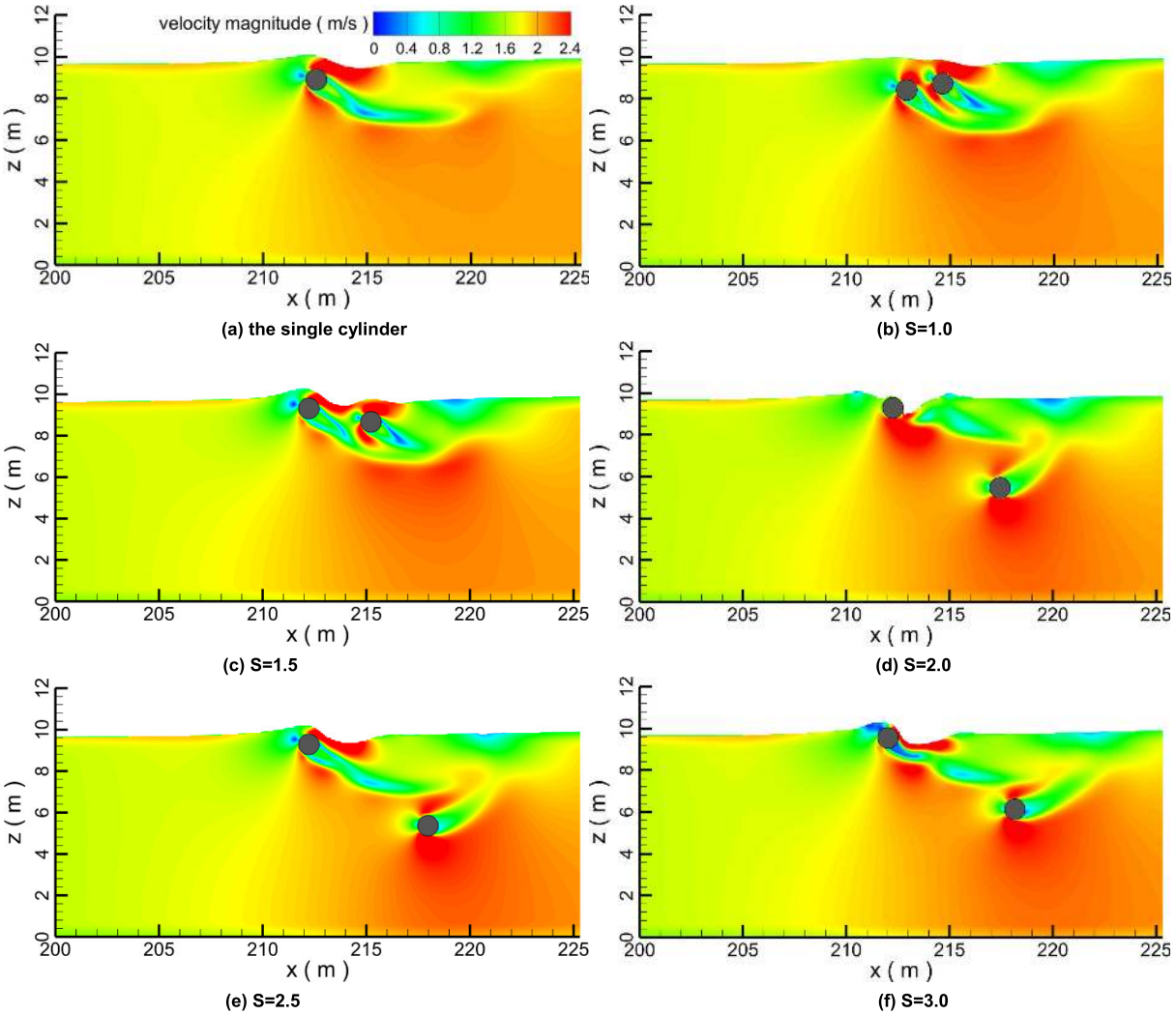

FIGURE 33. The velocity contours with different spacing ratios at the time of 144s.

and the flow velocity increase by degrees, when the preceding wave appears. The tandem cylinder continues to rise along the water surface and moves downstream with two detached vortices around (Fig. 31c). With the increase of the water elevation and current velocity of the secondary elevated wave, vortices behind the tandem cylinder become bigger and bigger (Fig. 31d). When the wave peak reaches the upstream cylinder, the upstream cylinder starts to oscillate and a pair of the detached vorticities is generated behind the cylinder (Fig. 31e). Along with the propagation of the wave, the oscillation of the downstream cylinder also occurs. When the downstream cylinder reaches the lowest point, the upstream cylinder has floated to the water surface. Two obvious vortices are behind the tandem cylinder, and the shapes of the vortices are consistent with the movement trajectories of two cylinders (Fig. 31f). Due to the vibration of the tandem cylinder, a much stronger interaction among the tandem cylinder, water surface and the shed vortices is noted (Fig. 31g and h). After the tsunami-like wave passes through the tandem cylinder site, the shed vortices are dissipated gradually and the cylinders move to the initial equilibrium position due to the tension of the mooring chains. It is also discovered that the whirlpool dissipates continuously (Fig. 31i). When the tsunami-like wave passes through the calculation domain around the tandem cylinder site, the water surface recorded at gauge B and the velocity recorded at sensor D are plotted in Figs. 30 and 32. Due to the disturbance of the floating tandem cylinder, both the water surface and the velocity fluctuate severely.

When the spacing ratio changes from 1.0 to 3.0, the snapshots of the velocity contour at the time of 144s are plotted in Fig. 33. Besides, the flow field of the velocity caused by the single cylinder at this time is also added for the comparison. When the peak of the tsunami-like wave arrives at the cylinder site, both the single cylinder and tandem cylinder oscillate in the water. When the spacing ratio S is less than 1.5, the oscillation trajectories of the tandem cylinders are similar and they are sinking and rising at the same time (Fig. 33a, b, and c).

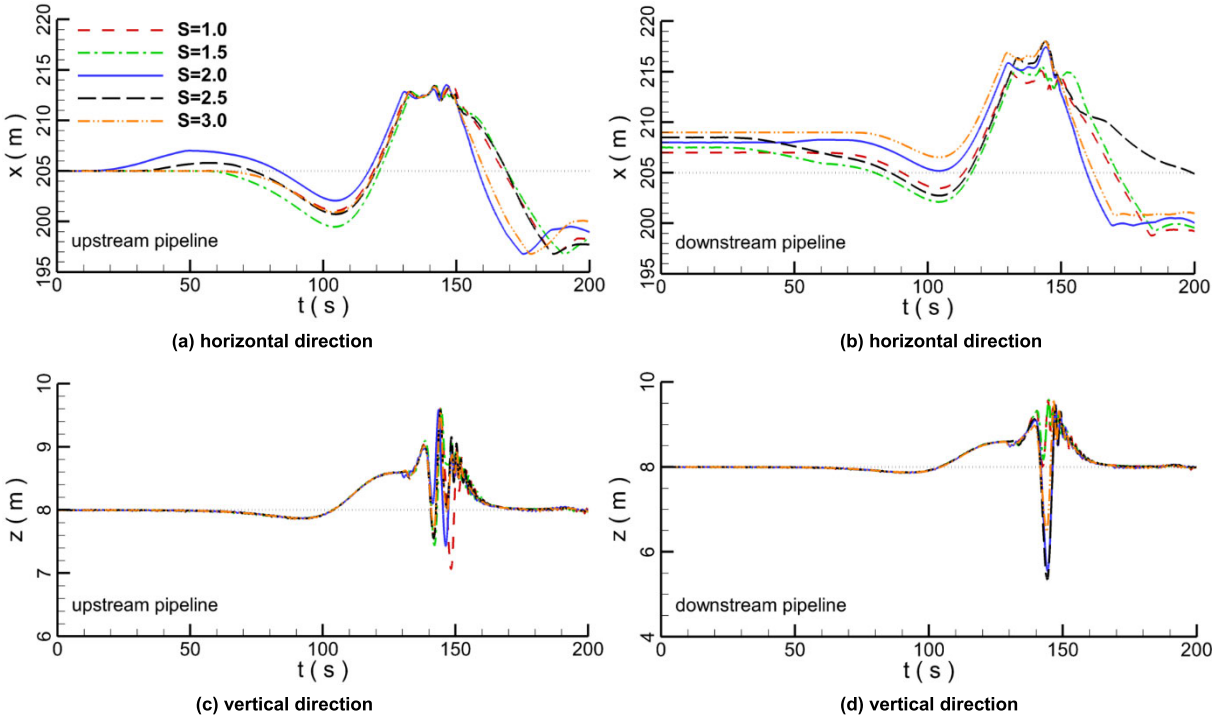

FIGURE 34. The movement trajectory of the cylinder.

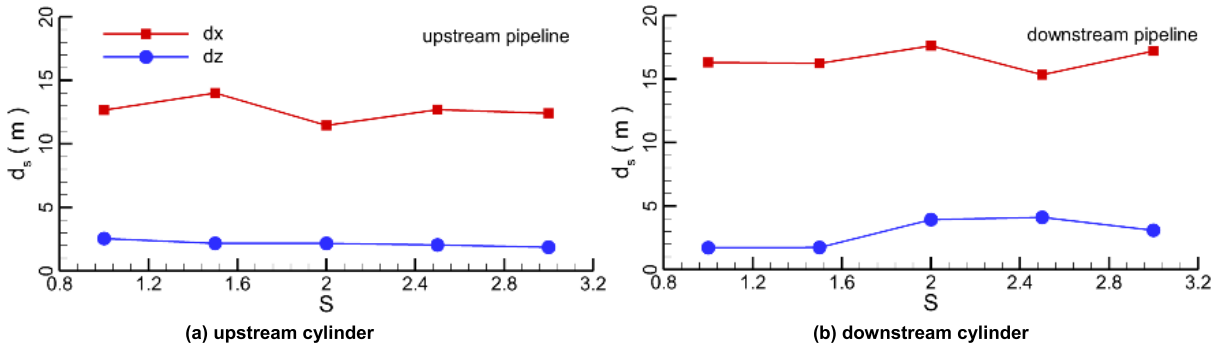

FIGURE 35. The maximum movement offsets of the cylinder at different spacing ratios.

When the spacing ratio S is larger than 1.5, the downstream cylinder is sinking but the upstream cylinder has reached the surface (Fig. 33d, e, and f), because with the increase of the spacing ratio S, the action time of the maximum hydrodynamic force on the downstream cylinder is delayed compared with the upstream cylinder. In the front and rear of the cylinder, the flow velocity is the smallest due to the effect of the cylinder obstruction. Correspondingly, at two sides of the cylinder, the velocity reaches maximum. The wave propagation is strongly disturbed by cylinder.

Motions of the tandem cylinder with different spacing ratios are given in Fig. 34. In the horizontal direction, both the upstream cylinder and downstream cylinder drift upstream firstly according to the depression wave and then move downstream according to the preceding wave and the secondary elevated wave (Fig. 34a and b). In the vertical direction, the sinking depth of the downstream cylinder is greater than that of the upstream cylinder (Fig. 34c and d). The maximum moving offsets of the tandem cylinder are illustrated in Fig. 35, showing that the horizontal displacement offsets of the upstream cylinder are smaller than those of the downstream cylinder at any spacing ratio. When the spacing ratio S is 2.0, in the horizontal direction, the offset of the upstream cylinder is minimum (Fig. 35a) but the offset of the downstream cylinder is the maximum (Fig. 35b). With the increase of the spacing ratio, the vertical offset of the upstream cylinder decreases but the offset of the downstream cylinder increases.

Fig. 36 depicts the corresponding temporal evolution of the total force exerted at floating tandem cylinder under

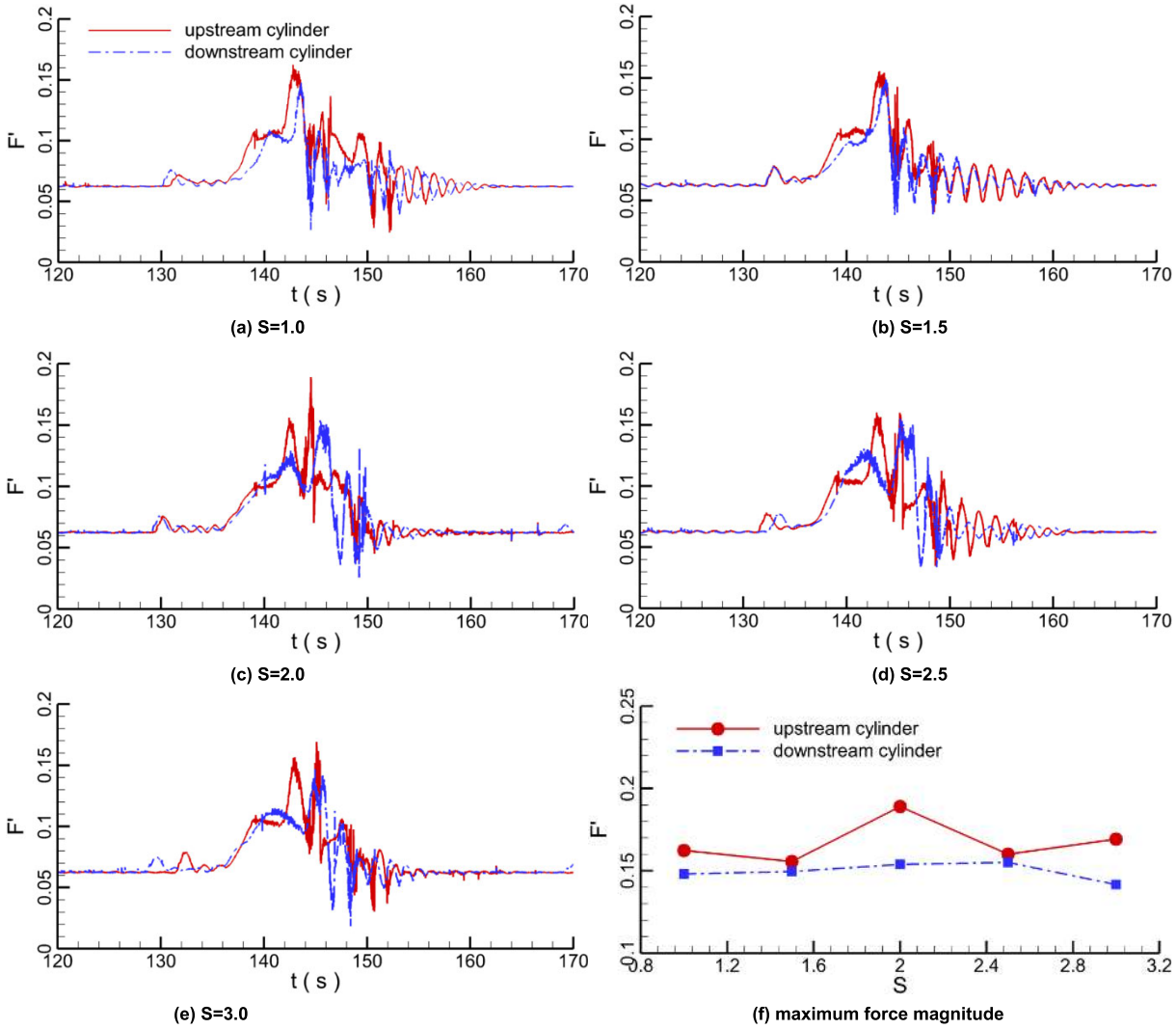

FIGURE 36. The force magnitude of the cylinder at different spacing ratios.

the tsunami-like wave with different cylinder spacing. When the peak of the tsunami-like wave arrives at the cylinder site, the force on the tandem cylinder exhibits a considerable oscillation. The temporal evolution of the force of the upstream cylinder nearly coincides with that of the downstream cylinder. Due to the strong vortices interaction between the upstream cylinder and the downstream cylinder, the temporal elevation of the force exerted at the cylinder vibrates severely with several peaks. After the tsunami-like wave passes through the cylinder site, the forces on the cylinder appear the periodic oscillation as a result of the damping between the cylinder and water surface. Finally, the cylinder is still on the surface of the water and the forces are not changed. The force magnitude of the upstream cylinder is always more than that of the downstream cylinder at different spacing ratios (Fig. 36f). When the spacing ratio S is 2.0, the force on the upstream is maximum, but when the spacing ratio S is 2.5, the force on the downstream cylinder is maximum. However, the change of the force is not significant. Overall, under the same tsunami-like wave, the effect of the spacing ratio on the force of cylinder is relatively weak.

The tension forces of the mooring chains with different spacing ratios are plotted in Fig. 37, in which the tension forces are generated by the drag of the moving cylinders. The tension forces of the upstream mooring chains (M1 and M3) are much more than that of the downstream mooring chains (M2 and M4) because the mooring chains mainly prevent the cylinders from moving downstream. Compared with the evolution of the forces of the cylinders, although the temporal evolution of the tension forces of the upstream mooring chains (M1 and M3) differ somewhat, the universal curve patterns are parallel. The tension forces of the mooring chains (M1 and M2) connecting the upstream cylinder keep very similar temporal evolution as that of the mooring chains (M3 and M4) connecting the downstream cylinder, although the tension forces still exhibit some oscillations. When the spacing ratio is 2.0, the tension force of the chain M1 reaches the maximum which is greater than that of the other chains,

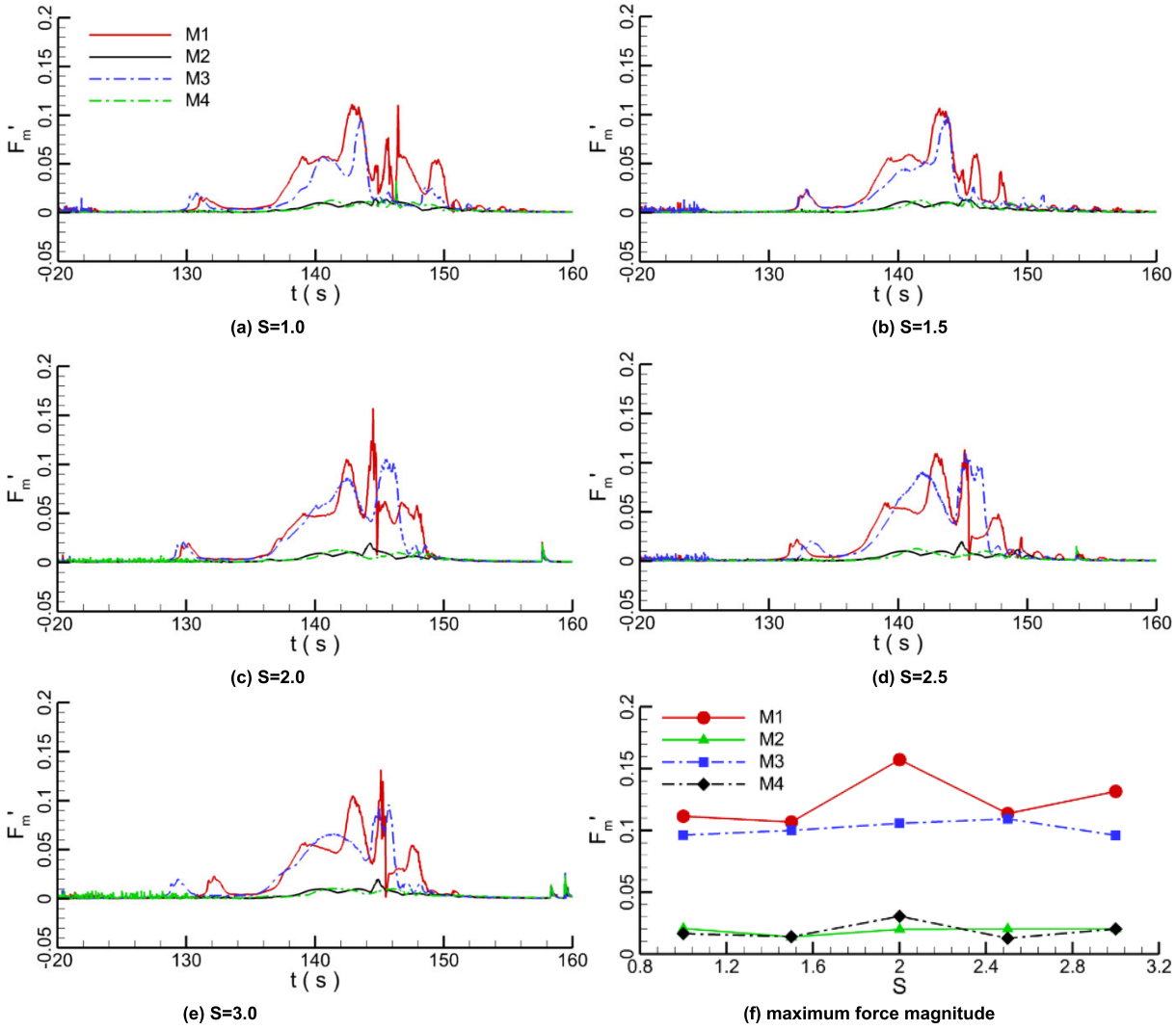

FIGURE 37. The force magnitude of the mooring chain at different spacing ratios.

shown in Fig. 37f. In a word, the tension forces of the mooring chains are linked to the movement of the cylinder. The spacing ratio has no significant influence on the cylinder movement, so the tension forces of the mooring chains restricting the movement of the cylinder do not change greatly at different ratios.

V. CONCLUSION

This paper numerically investigates the effects of the tsunami-like wave on moored floating cylinders which are common structural components for ocean and coastal infrastructures. According to the real-world tsunami wave profile recorded during the 2011 Japan Tohoku tsunami, the tsunami-like wave is generated in a numerical wave tank based on incompressible Navier-Stokes equations and VOF method. In order to analyze the difference of hydrodynamic characteristics between the solitary wave and the tsunami-like wave, numerical simulations of the interactions between the two waves and moored cylinders are conducted. Additionally, the effects of the tsunami-like wave on the different single and tandem cylinders are also considered. Main conclusions drawn in this research can be summarized as follows:

(1) When the wave passes through the cylinder, the wave profile and velocity are changed due to the interference of the cylinder. The wave height of the tsunami-like wave and the solitary wave reduce about 1.7% and 3.8% respectively, revealing that the wave energy of the solitary wave is more absorbed than that of the tsunami-like wave. At the identical still water depth and wave height, the motions and motion range of the cylinder under the tsunami-like wave are larger than that under the solitary wave in both horizontal and vertical directions. Compared with the solitary wave, the tsunami-like wave can cause 1.5 times greater force on the cylinder with a significant long acting duration, correspondingly, the tension forces of the mooring chains under the tsunami-like wave is also much greater. It is also observed that the cylinder drifts upstream when the depression wave portion of the tsunami-like wave approaches the cylinder on

account of the decrease of the water elevation. When the secondary elevated wave arrives at the cylinder, the cylinder oscillates severely and the vortex sheds strongly with the oscillation of the cylinder, however, motion of the cylinder under the solitary wave is much weaker. Overall, compared with the solitary wave, the wave profile of the tsunami-like wave includes three wave portions. The period, wave length and wave velocity magnitude of the tsunami-like wave are all more than that of the solitary wave. The vortex behind the cylinder under the tsunami-like wave shakes and sheds more complex than that of the solitary. When the cylinder moves in the wave, the maximum displacement of the cylinders under the tsunami-like wave and the solitary wave are close because of the restriction of the mooring chains. Therefore, it is seen that based on the more realistic tsunami wave, the hydrodynamic characteristics of the interaction between the tsunami-like wave and the cylinder are much different to the ones of the interaction between the solitary wave and the cylinder.

(2) When the tsunami-like wave impinges on the moored cylinder, the vertical motion of the cylinder decreases with the increase of the cylinder diameter, which means that the larger the structure in the ocean is, the smaller the amplitude of the cylinder vibration would be. Furthermore, with the increase of cylinder diameter, the dimensionless hydrodynamics forces on the cylinder decrease monotonously but the tension forces of the mooring lines increase on the contrary. After the wave takes place in the cylinder site, the vortex shed behind the cylinder grows bigger with the increase of the cylinder diameter.

(3) When cylinders in tandem arrangement are considered, there is a strong interaction among the upstream cylinder, downstream cylinder and the water surface. If the spacing ratio S is less than 1.5, the oscillation trajectories of the upstream and downstream cylinders are similar. The shed vortices of the upstream cylinder act directly on the downstream cylinder. However, if the spacing ratio S is larger than 1.5, the movement of both cylinders is not synchronized. With the increase of the spacing ratio, the influence of the shed vortices on the downstream pipeline gradually decreases. When the peak of the tsunami-like wave arrives at the cylinder site, the peak value of the force on the upstream cylinder is larger than that of the downstream cylinder. Moreover, the tension forces of the upstream mooring chains (M1 and M3) are much more than that of the downstream mooring chains (M2 and M4) due to the mooring chains (M1 and M3) mainly prevent the cylinders from moving downstream.

The authors believe that the conclusions drawn from this work might provide practical reference to the understanding of the real-world tsunami wave and the hydrodynamic characteristics of the interaction between tsunami waves and cylinder structures, which could be helpful to the design of coastal and offshore infrastructures in the engineering field. In the further research, it is suggested that the real-world tsunami wave is generated experimentally. Moreover, the hydrodynamics characteristics of the interaction between tsunami waves and more complex offshore structures are worth studying.

REFERENCES

[1] H. Takagi and J. D. Bricker, "Assessment of the effectiveness of general breakwaters in reducing tsunami inundation in Ishinomaki," *Coast Eng. J.*, vol. 56, pp. 1450018-1–1450018-21, Nov. 2014.

[2] T. Tomita, G.-S. Yeom, M. Ayugai, and T. Niwa, "Breakwater effects on tsunami inundation reduction in the 2011 off the pacific coast of Tohoku earthquake," *J. Jpn. Soc. Civil Eng.*, vol. 68, no. 2, pp. 156–160, 2012.

[3] J. Yu, A. M. Cruz, E. Piatyszek, M. Lesbats, A. Tardy, A. Hokugo, and H. Tatano, "A survey of impact on industrial parks caused by the 2011 great east Japan earthquake and tsunami," *J. Loss Prevention Process Ind.*, vol. 50, pp. 317–324, Nov. 2017.

[4] T. Rossetto, W. Allsop, I. Charvet, and I. D. Robinson, "Physical modelling of tsunami using a new pneumatic wave generator," *Coastal Eng.*, vol. 58, pp. 517–527, Jun. 2011.

[5] N. Goseberg, A. Wurpts, and T. Schlurmann, "Laboratory-scale generation of tsunami and long waves," *Coastal Eng.*, vol. 79, pp. 57–74, Sep. 2013.

[6] W. Allsop, I. Chandler, and M. Zaccaria, "Improvements in the physical modelling of tsunamis and their effects," in *Proc. 5th Int. Conf. Appl. Phys. Modeling Port Coastal Protection*, 2014, pp. 1–22.

[7] G. C. Bremm, N. Goseberg, T. Schlurmann, and I. Nistor, "Long wave flow interaction with a single square structure on a sloping beach," *J. Marine Sci. Eng.*, vol. 3, no. 3, pp. 821–844, 2015.

[8] D. J. McGovern, T. Robinson, I. D. Chandler, W. Allsop, and T. Rossetto, "Pneumatic long-wave generation of tsunami-length waveforms and their runup," *Coastal Eng.*, vol. 138, pp. 80–97, Aug. 2018.

[9] D. Liang, H. Gotoh, A. Khayyer, and J. M. Chen, "Boussinesq modelling of solitary wave and N-wave runup on coast," *Appl. Ocean Res.*, vol. 42, pp. 144–154, Aug. 2013.

[10] G. Tripepi, F. Aristodemo, P. Veltri, C. Pace, A. Solano, and C. Giordano, "Experimental and numerical investigation of tsunami-like waves on horizontal circular cylinders," in *Proc. Int. Conf. Ocean, Offshore Arctic Eng. ASME*, 2017, Art. no. V07AT06A056.

[11] F. Aristodemo, G. Tripepi, D. D. Meringolo, and P. Veltri, "Solitary wave-induced forces on horizontal circular cylinders: Laboratory experiments and SPH simulations," *Coastal Eng.*, vol. 129, pp. 17–35, Nov. 2017.

[12] Í. Aniel-Quiroga, C. Vidal, J. L. Lara, M. González, and Á. Sainz, "Stability of rubble-mound breakwaters under tsunami first impact and overflow based on laboratory experiments," *Coastal Eng.*, vol. 135, pp. 39–54, May 2018.

[13] T. Ha, J. Shim, P. Lin, and Y.-S. Cho, "Three-dimensional numerical simulation of solitary wave run-up using the IB method," *Coastal Eng.*, vol. 84, pp. 38–55, Feb. 2014.

[14] H. Kawai, M. Satoh, K. Kawaguchi, and K. Seki, "Characteristics of the 2011 Tohoku tsunami waveform acquired around Japan by NOWPHAS equipment," *Coastal Eng. J.*, vol. 55, Sep. 2013, Art. no. 1350008.

[15] P. A. Madsen, D. R. Fuhrman, and H. A. Schäffer, "On the solitary wave paradigm for tsunamis," *J. Geophys. Res.*, vol. 113, pp. 286–292, Dec. 2008.

[16] P. A. Madsen and H. A. Schäffer, "Analytical solutions for tsunami runup on a plane beach: Single waves, N-waves and transient waves," *J. Fluid Mech.*, vol. 645, pp. 27–57, Feb. 2010.

[17] I.-C. Chan and P. L.-F. Liu, "On the runup of long waves on a plane beach," *J. Geophys. Res.*, vol. 117, pp. 72–82, Aug. 2012.

[18] I. A. Williams and D. R. Fuhrman, "Numerical simulation of tsunami-scale wave boundary layers," *Coastal Eng.*, vol. 110, pp. 17–31, Apr. 2016.

[19] K. Qu, X. Y. Ren, S. Kraatz, and E. J. Zhao, "Numerical analysis of tsunami-like wave impact on horizontal cylinders," *Ocean Eng.*, vol. 145, pp. 316–333, Nov. 2017.

[20] P. Wadhams, "A mechanism for the formation of ice edge bands," *J. Geophys. Res.*, vol. 88, pp. 2813–2818, Mar. 1983.

[21] Z. Zang, B. Teng, W. Bai, and L. Cheng, "A finite volume solution of wave forces on submarine pipelines," *Ocean Eng.*, vol. 34, no. 14, pp. 1955–1964, Oct. 2007.

[22] H. Qin, W. Tang, H. Xue, Z. Hu, and J. Guo, "Numerical study of wave impact on the deck-house caused by freak waves," *Ocean Eng.*, vol. 133, pp. 151–169, Mar. 2017.

[23] C. M. Rhie and W. L. Chow, "Numerical study of the turbulent flow past an airfoil with trailing edge separation," *AIAA J.*, vol. 21, no. 11, pp. 1525–1532, 1983.

[24] R. I. Issa, "Solution of the implicitly discretised fluid flow equations by operator-splitting," *J. Comput. Phys.*, vol. 62, pp. 40–65, Jan. 1986.
[25] M. Darwish and F. Moukalled, "Convective schemes for capturing interfaces of free-surface flows on unstructured grids," *Numer. Heat Transf. Fundam.*, vol. 49, no. 1, pp. 19–42, 2006.
[26] J. W. Miles, "Solitary waves," *Annu. Rev. Fluid Mech.*, vol. 12, no. 1, pp. 11–43, 1980.
[27] D. Stanisic, M. Efthymiou, M. Kimiaei, and W. Zhao, "Design loads and long term distribution of mooring line response of a large weathervaning vessel in a tropical cyclone environment," *Marine Struct.*, vol. 61, pp. 361–380, Sep. 2018.
[28] M. Borg, M. Collu, and A. Kolios, "Offshore floating vertical axis wind turbines, dynamics modelling state of the art. Part II: Mooring line and structural dynamics," *Renew. Sust. Energ. Rev.*, vol. 39, pp. 1226–1234, Nov. 2014.
[29] O. A. Montasir, A. Yenduri, and V. J. Kurian, "Effect of mooring line configurations on the dynamic responses of truss spar platforms," *Ocean Eng.*, vol. 96, pp. 161–172, Mar. 2015.
[30] G. Huang, A. W.-K. Law, and Z. Huang, "Wave-induced drift of small floating objects in regular waves," *Ocean Eng.*, vol. 38, pp. 712–718, Mar. 2011.
[31] P. O. Sibley, "The solitary wave and the forces it imposes on a submerged horizontal circular cylinder: An analytical and experimental study," Ph.D. dissertation, City Univ. London, London, U.K., 1991.
[32] *Ships and Marine Technology-Mooring Chain*, ISO Standard 20438, Asian Star Anchor Chain, Nanjing, China, 2016.

ENJIN ZHAO received the B.S. and Ph.D. degrees from the College of Engineering, Ocean University of China, Qingdao, China, in 2012 and 2017, respectively. He is currently with the College of Marine Science and Technology, China University of Geosciences, Wuhan, China. His research interests include ocean engineering and marine technology.

JUNKAI SUN received the B.E. degree in civil engineering from the China University of Geosciences, Wuhan, China, in 2018, where he is currently a postgraduate student of science in ocean engineering. His research interests include ocean structure scour and dynamic response analysis.

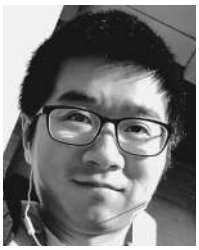

HAOYU JIANG was born in China, in 1989. He received the Ph.D. degree in ocean remote sensing from the Ocean University of China, Qingdao, China, in 2017. He is currently an Associate Professor with the College of Marine Science and Technology, China University of Geosciences, Wuhan, China. His research interests include oceanic remote sensing and wind waves, as well as their applications to ocean engineering.

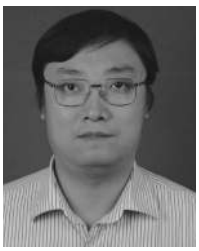

LIN MU received the B.S., M.S., and Ph.D. degrees in physical oceanography from the Ocean University of China, Qingdao, China, in 2000, 2002, and 2007, respectively. He is currently a Professor and Ph.D. Supervisor of physical oceanography with the China University of Geosciences, Wuhan, China. He has authored or coauthored over 20 scientific papers and three books. His research interests include physical oceanography: prevention and mitigation of marine disasters, maritime search and rescue, and emergency response management of offshore oil spills.